International Journal of Heat and Mass Transfer 52 (2009) 932–951

Contents lists available at ScienceDirect

International Journal of Heat and Mass Transfer

journal homepage: www.elsevier.com/locate/ijhmt

Pulsating convective cooling across two porous-covering heated blocks

Po-Chuan Huang [a,*], Yen-Jen Chen [a], Meir-Chyun Tzou [b]

[a] Department of Energy and Refrigerating Air-Conditioning Engineering, National Taipei University of Technology, Taipei 106, Taiwan, ROC
[b] Bureau of Food and Drug Analysis, Department of Health, Executive Yuan, Taipei 11513, Taiwan, ROC

ARTICLE INFO

Article history:
Received 12 September 2007
Received in revised form 30 May 2008
Available online 11 September 2008

ABSTRACT

A numerical study has been undertaken to analyze the flow and thermal characteristics of forced pulsating flow through a channel with two porous-covering heated blocks in tandem. Solution of the coupled governing equations for the fluid/porous/solid composite system is obtained by utilizing a control-volume method through the use of a stream function-vorticity approach. This study details the effects of variations in the Darcy number, pulsation frequency and amplitude, three pertinent geometric parameters and effective conductivity ratio, to illustrate important fundamental and practical results. The results show that the periodic alteration in the structure of recirculation flow inside the inter-block region and behind the downstream block significantly enhances the heat transfer rate on the block right faces.

1. Introduction

Thermal control of electronic equipment and devices has received considerable attention by investigators in the past decades due to the requirement of maintenance of relatively constant temperature equal to or below a maximum operating temperature. In response to these demands, different techniques have been used in the past to obtain a well-controlled thermal environment, including a variety of passive or active enhanced cooling techniques. Among the heat transfer enhancement schemes, one of the promising techniques is the application of a porous medium subjected to flow pulsation. The porous medium has emerged as an effective passive cooling enhancer due to the high ratio of surface area to volume ratio in the heat transfer process and intense flow mixing, caused by the tortuous path of the porous matrix, in the thermal dispersion process. The forced pulsation of incoming fluid at the entrance of channel is another active augmenting method due to the hydrodynamic instability in a shear layer, which substantially increases lateral, large-scale flow mixing and hence augments the convective thermal transport in the direction normal to the heated surface.

The problem of convective heat transfer in fluid-saturated porous media has been a major topic for various studies during the past decades due to its relevance in a wide range of application such as thermal insulation engineering, water movements in geothermal reservoirs, nuclear waste repository, heat pipe, grain storage, etc. Extensive studies have been conducted on the steady forced convection flow through a channel fully or partially filled with a porous material as a heat sink for heat transfer augmentation. Koh and Colony [1] analyzed the cooling effectiveness for a porous material in a cooling passage. Kaviany [2] dealt with convective heat transfer from a steady laminar flow through a porous channel bounded by two isothermal parallel plates. Huang and Vafai [3] simulated steady forced convection problem in an isothermal parallel plate channel with porous block array. Angirasa [4] numerically reported forced convection in a channel filled with metallic fibrous materials. Their results showed that porous substrate substantially enhance the thermal performance in a channel. Recently, the forced convection heat transfer in a fully/partially porous channel with discrete heated sources or blocks was of special interest due to its applications on the microelectronic cooling. Hadim and Bethancourt [5] investigated forced convection in fully/partially porous channel containing discrete heat sources on the bottom wall. A significant increase in heat transfer rate was observed, as the Darcy number was decreased, especially at the leading edge of each heat source. Angirasa and Peterson [6] numerically studied forced convection heat transfer augmentation in a channel with a localized heat source using metal fibrous material. They concluded that thinner fibers and high porosity media enhance heat transfer because of better distribution flow and mixing. Fu et al. [7] investigated heat transfer from a spherical-bead porous-block-mounted heated wall in a channel flow. They reported that for the blocked ratio $H_p^* = 0.5$ the thermal performances are enhanced at higher porosity and porous particle diameter. However, the result is opposite for $H_p^* = 1$. Huang et al. [8] analyzed forced convective heat transfer from multiple heated blocks in a channel by porous covers and found that the recirculation caused by porous-covering block will significantly augment the heat transfer rate on both top and right faces of second and subsequent blocks.

* Corresponding author. Tel.: +886 2 27712171x3514; fax: +886 2 27314919.
E-mail address: pchuang@ntut.edu.tw (P.-C. Huang).

0017-9310/$ - see front matter © 2008 Elsevier Ltd. All rights reserved.
doi:10.1016/j.ijheatmasstransfer.2008.07.026

Nomenclature

A	oscillating amplitude of axial inlet velocity
C_p	specific heat at constant pressure (J/kg K)
Da	Darcy number, K/R^2
f	dimensional forcing frequency (Hz)
F	function used in expression inertia terms
h	convective heat transfer coefficient (W/m^2 K)
H	height (m)
k	thermal conductivity (W/m K)
K	permeability of the porous medium (m^2)
L	length (m)
Nu_m	cycle-space average overall mean Nusselt numbers, Eq. (14)
Nu_x	cycle-averaged local Nusselt number, Eq. (13)
Nu_{xt}	local instantaneous Nusselt number, Eq. (12)
P	pressure (N/m^2)
Pe	Pelect number, u_oR/α
Pr	Prandtl number, ν/α
q''	uniform heat flux from each heated block (W/m^2)
R	height of channel (m)
Rc	heat capacity ratio, $(\rho C_p)/(\rho C_p)_f$
R_k	thermal conductivity ratio, k/k_f
Re	Reynolds number, u_oR/ν
S	spacing between heat sources or porous blocks (m)
St	dimensionless pulsating frequency, Strouhal number, fR/u_o
t	time (s)
T	temperature (K)
u_o	cycle-averaged velocity of the inlet flow (m/s)
u, v	velocity component (m/s)
V	velocity vector (m/s)
W	width (m)
x, y	Cartesian coordinates (m)

Greek symbols

α	thermal diffusivity (m^2/s)
δ	boundary layer thickness (m)
ε	porosity of the porous medium
Λ	inertial parameter, $F\varepsilon^2/\sqrt{Da}$
κ	tangential direction
μ	dynamic viscosity (kg/ms)
ν	kinematic viscosity (m^2/s)
ξ	vorticity (1/s)
ρ	density (kg/m^3)
τ	oscillatory period for a cycle
Π	overall exposed area of a block (m^2)
ϕ	stream function (m^2/s)
ω	angular velocity (1/s)

Superscript

*	dimensionless quantity

Subscripts

eff	effective
f	fluid
i	inlet
p	porous
o	outlet
s	non-pulsating component, or solid
x	local
t	total

More recently, due to the needs of high-performance high-power electronic devices, there has been an increasing demands to achieve higher heat transfer removal from the fully/partially porous channel flow. One of such efforts has been given to explore the use of porous heat sink subjected to pulsation flow. Here, a pulsating channel flow, i.e., an oscillating component superposed on the mean flow in a confined passage, can enhance the axial transfer of energy due to large oscillating temperature gradients in the direction normal to the heated wall. Pulsating flow is frequent encountered in natural system (human respiratory and vascular system) and engineering system (exhaust and intake manifolds of IC engines, regenerator, Stirling engine, electronic cooling, etc.). For the related heat transfer characteristics studies of pulsating confined flow over protruding blocks or fins, Mackley and Ni [9], Nishimura et al. [10], and Azar [11] pointed out that fluid mixing and heat transfer are intensified by fluid oscillation in furrowed-wall channels and baffled tubes. However, published studies on pulsating convective flow passing through porous channel are scarce. Kim et al. [12] simulated forced pulsating flow in a fully porous channel. The results showed that the effect of pulsation on heat transfer between the channel wall and fluid is more pronounced in case of small pulsating frequency and large pulsating amplitude. Khodadadi [13] analyzed a fully developed oscillatory flow through a porous medium channel bounded by two impermeable parallel plates, showing that the velocity profiles exhibit maxima next to the wall. Paek et al. [14] performed an experimental study of pulsating flow through a porous duct. It was indicated that the heat transport from the porous material decreases as pulsating frequency decreases at given amplitude and is decreased when the pulsating amplitude is large enough to cause a backward flow. Fu et al. [15] conducted experimentally the heat transfer of a porous channel subjected to oscillating flow and found that the length-average Nusselt number for oscillating flow is higher than that for steady flow. Leong and Jin [16] treated experimentally the heat transfer in oscillating flow through a channel filled with an aluminum foam subjected a constant wall heat flux. Their results revealed that the heat transfer in oscillating flow is significantly enhanced by employing porous media in a plate channel. Most of these studies are related to the aspect of forced-pulsation convection over the full-porous system, however, little is known about the problem combining forced pulsating convection in a fluid/porous composite system and conduction in the solid region due to the complex geometry and the different thermal properties among the composite system. This constitutes a case for forced pulsating convection over a fluid/porous/solid composite system, such as a finite-sized porous substance enclosing a block where the block is used to simulate heated electronic component while the porous cover simulate the porous heat sink. Guo et al. [17] investigated the pulsating flow and heat transfer in a partially porous pipe and indicated the maximum effective thermal diffusivity was gained by pulsating flow through a pipe partially filled with porous medium rather than the limiting case of no porous medium or the fully filling of porous medium. The purpose of the present study is to explore the effects of both the heat transfer enhancement factors by external flow pulsation and finite-size fiber porous cover on the convective cooling of electronic devices.

This paper describes a numerical investigation on flow field and heat transfer characteristics of two successive porous-covering

heated blocks subjected to pulsating channel flow. Both the mixing enhanced convection caused by porous cover and the oscillatory enhanced convection caused by pulsating flow are examined. Several important characteristic of the time-dependent flow and temperature fields in the fluid/porous/solid composite system is reported. The dependence of these characteristics on the governing parameters such as Darcy number, pulsation frequency and amplitude, and effective conductivity ratio is also documented. In addition, the results are also compared with those obtained for a steady non-pulsating nonporous-cover flow. It is shown that altering some parametric values can have significant and interesting effects on the cooling of the heat blocks.

2. Mathematical formulation

The configuration of problem under investigation is depicted in Fig. 1(a). It includes flow through a parallel-plate channel with two porous-covering heated blocks on the bottom plate. Both upper and lower channel walls are insulated. The fluid enters the channel at uniform temperature T_i with a pulsating flow $u_i = u_o[1 + A\sin(\omega t)]$, where A and ω are the pulsating amplitude and frequency, respectively. The flow field is assumed to be unsteady, two-dimensional, laminar, and incompressible. Buoyancy induced effects are assumed negligible, and the heat generation within the blocks is assumed to be constant and uniform. Besides, the thermophysical properties of the fluid and the porous matrix are assumed to be constant, and the fluid-saturated porous medium is considered homogeneous, isotropic, non-deformable, and in local thermodynamic equilibrium with the fluid. Possible channelling near the wall is neglected in the present study because fibrous media are considered for which the porosity and permeability are relatively constant even close to the wall (Hunt and Tien [18]). The effective viscosity of porous medium is equal to the viscosity of the fluid. In this work, the flow is modelled by the time-dependent Darcy–Brinkman–Forchheimer equation in the porous matrix to incorporate the viscous and inertial effects (Vafai and Tien [19]) and by transient Navier–Stokes equation in the fluid domain, and the thermal field by the energy equation. Then, an efficient alternative method for combining the three sets of governing equations for the fluid, porous, and solid regions into one set of conservation equations is to model the whole fluid/porous/solid composite system as a single domain governed by one set of conservations, the solution of which satisfies the matching conditions at both fluid/porous and porous/solid interfaces. The above-mentioned resulting unsteady momentum and energy equations in terms of dimensionless variables are as followings (Huang and Vafai [3], Huang et al. [20]):

$$\varepsilon\frac{\partial\zeta^*}{\partial t^*} + u^*\frac{\partial\zeta^*}{\partial x^*} + v^*\frac{\partial\zeta^*}{\partial y^*} = \frac{\varepsilon}{Re}\nabla^2\zeta^* + S^*_\phi \tag{1}$$

$$\nabla^2\varphi^* = -\xi^* \tag{2}$$

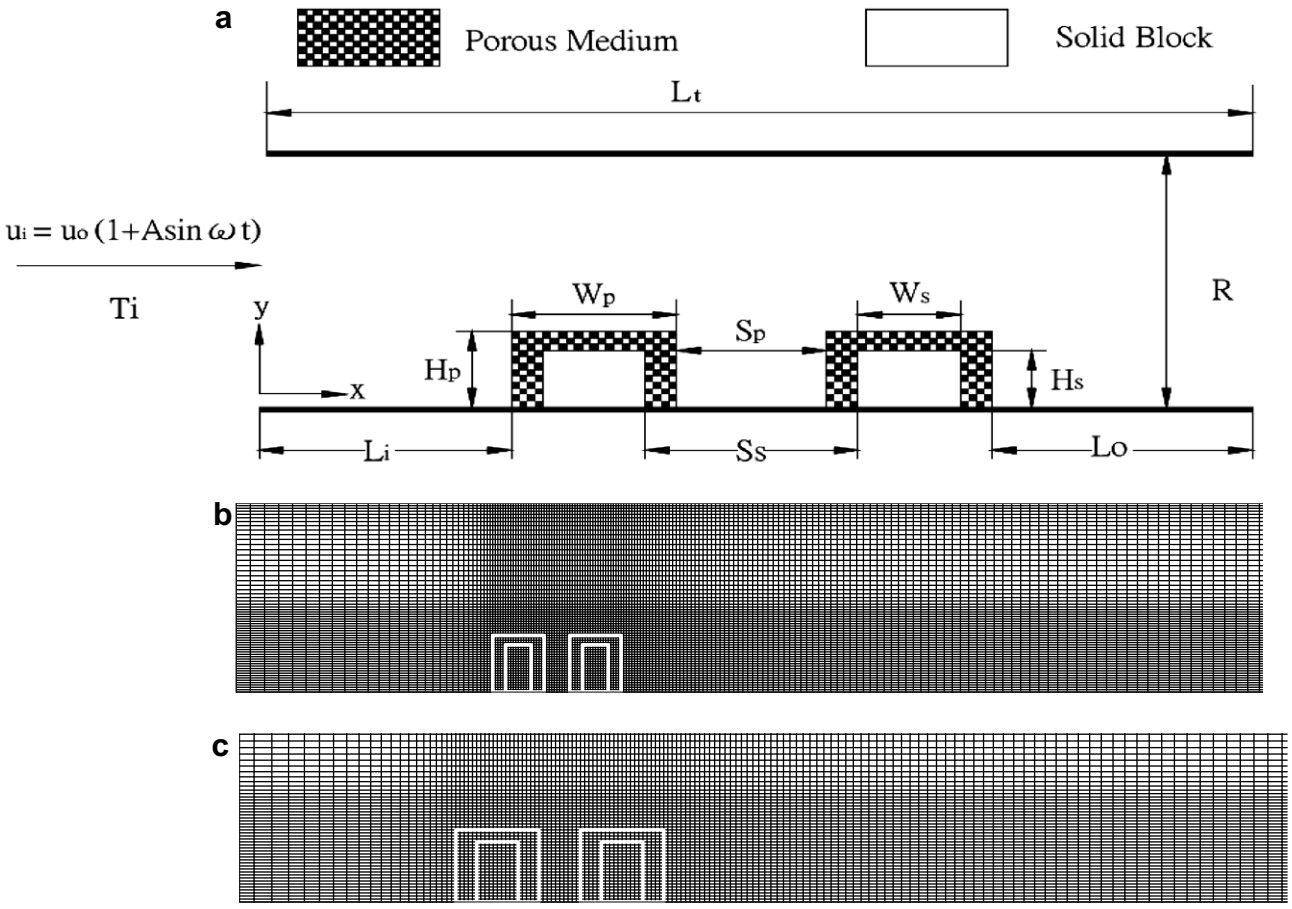

Fig. 1. (a) Schematic diagram of the problem and the corresponding coordinate systems, (b) a typical nonuniform grid system for the whole computational domain, and (c) a close-up of the region near the porous-covering heated block.

$$Pe\left(Rc\frac{\partial T^*}{\partial t^*}+u^*\frac{\partial T^*}{\partial x^*}+v^*\frac{\partial T^*}{\partial y^*}\right)=\nabla\cdot(R_k\nabla T^*)+\frac{\vartheta}{H^*\cdot W^*} \tag{3}$$

where (x^*,y^*) are dimensionless rectangular Cartesian coordinates, ε is the porosity of the porous medium, Re is Reynolds number, Pe is the Pelect number, Rc is the heat capacity ratio, R_k is the thermal conductivity ratio, and S^*_φ is the source term. ϑ is a function set equal to one to account for heat generation in the block, and to zero elsewhere, and ϕ and ξ are the stream function and vorticity, respectively, which are related to the fluid velocity components u and v by

$$u=\frac{\partial\varphi}{\partial y},\quad v=-\frac{\partial\varphi}{\partial x},\quad \xi=\frac{\partial v}{\partial x}-\frac{\partial u}{\partial y} \tag{4}$$

The non-dimensional parameters in the fluid region are

$$\begin{aligned}&Rc_{\mathrm{f}}=(\rho C_{\mathrm{p}})_{\mathrm{f}}/(\rho C_{\mathrm{p}})_{\mathrm{f}}=1,\quad Re_{\mathrm{f}}=u_{\mathrm{o}}R/\nu_{\mathrm{f}},\quad Pe_{\mathrm{f}}=u_{\mathrm{o}}R/\alpha_{\mathrm{f}},\\&R_{\mathrm{kf}}=k_{\mathrm{f}}/k_{\mathrm{f}}=1,\quad S^*_\varphi=0,\quad \varepsilon=1,\quad \vartheta=0\end{aligned} \tag{5}$$

and in the porous region the non-dimensional parameters are

$$\begin{aligned}&Rc_{\mathrm{eff}}=(\rho C_{\mathrm{p}})_{\mathrm{eff}}/(\rho C_{\mathrm{p}})_{\mathrm{f}},\quad Re_{\mathrm{eff}}=u_{\mathrm{o}}R/\nu_{\mathrm{eff}},\quad Pe_{\mathrm{eff}}=u_{\mathrm{o}}R/\alpha_{\mathrm{eff}},\\&R_{\mathrm{keff}}=k_{\mathrm{eff}}/k_{\mathrm{f}}\end{aligned} \tag{6a}$$

$$\begin{aligned}S^*_\varphi=&-\frac{\varepsilon^2}{Re_{\mathrm{eff}}Da}\zeta^*-\frac{F\varepsilon^2}{\sqrt{Da}}|\overline{V}^*|\zeta^*\\&-\frac{F\varepsilon^2}{\sqrt{Da}}\left[v^*\frac{\partial|\overline{V}^*|}{\partial x^*}-u^*\frac{\partial|\overline{V}^*|}{\partial y^*}\right],\quad \vartheta=0\end{aligned} \tag{6b}$$

where the Darcy number, $Da = K/R^2$, is related to the permeability of the porous medium. F is the inertia coefficient of porous medium and k_{eff} is the effective thermal conductivity of fluid-saturated porous medium. The energy equation for solid blocks becomes

$$Pe_{\mathrm{f}}\left(Rc_{\mathrm{s}}\frac{\partial T^*}{\partial t^*}\right)=\nabla\cdot(R_{\mathrm{ks}}\nabla T^*)+\frac{\vartheta}{H^*\cdot W^*} \tag{7}$$

where $Rc_{\mathrm{s}} = (\rho C_p)_s/(\rho C_p)_{\mathrm{f}}$, $R_{\mathrm{ks}} = k_s/k_{\mathrm{f}}$ (taken equal to 10 in the present study), $\vartheta = 1$. The source term S^*_φ can be considered as those contributing to the vorticity generation due to the presence of the rectangular porous-covering blocks. All of the above variables have been non-dimensionalized based on the following definitions:

$$\begin{aligned}&x^*=\frac{x}{R},\quad y^*=\frac{y}{R},\quad u^*=\frac{u}{u_{\mathrm{o}}},\quad v^*=\frac{v}{u_{\mathrm{o}}},\\&|\overline{V}^*|=\sqrt{u^{*2}+v^{*2}},\quad L^*=\frac{L}{R},\quad H^*_{\mathrm{p}}=\frac{H_{\mathrm{p}}}{R},\quad W^*_{\mathrm{p}}=\frac{W_{\mathrm{p}}}{R}\end{aligned} \tag{8a}$$

$$\begin{aligned}&H^*_{\mathrm{s}}=\frac{H_{\mathrm{s}}}{R},\quad W^*_{\mathrm{s}}=\frac{W_{\mathrm{s}}}{R},\quad S^*_{\mathrm{s}}=\frac{S_{\mathrm{s}}}{R},\quad S^*_{\mathrm{p}}=\frac{S_{\mathrm{p}}}{R},\quad \varphi^*=\frac{\varphi}{u_{\mathrm{i}}R},\\&\xi^*=\frac{R\xi}{u_{\mathrm{i}}}\end{aligned} \tag{8b}$$

$$St=\frac{fR}{u_{\mathrm{o}}},\quad t^*=\frac{tu_{\mathrm{o}}}{R},\quad T^*=\frac{T-T_{\mathrm{i}}}{q''R/k_{\mathrm{f}}},\quad Pr=\frac{\nu}{\alpha},\quad P^*=\frac{P}{\rho u_{\mathrm{o}}^2} \tag{8c}$$

It should be noted that these conservation equations for forced convection in the porous region are developed here using the local volume-averaging technique (Vafai and Tien [19]).

The associated dimensionless initial and boundary conditions necessary to complete the formulation of the present problem are:

(1) At the channel($x^* = 0,\ 0 < y^* < 1,\ t^* > 0$), the unidirectional, pulsating flow inlet is given

$$\varphi^*=y^*,\quad \xi^*=0,\quad T^*=0,\quad u^*=1+A\sin(2\pi Stt^*),\quad v^*=0 \tag{9a}$$

(2) At the exit ($x^* = L^*_{\mathrm{t}}, 0 < y^* < 1, t^* > 0$), the fully developed conditions is satisfied

$$\frac{\partial\varphi^*}{\partial x^*}=0,\quad \frac{\partial\xi^*}{\partial x^*}=0,\quad \frac{\partial T^*}{\partial x^*}=0 \tag{9b}$$

(3) Along the channel walls, the no-slip conditions at the perfect-insulated plates are taken. Namely, along the lower plate ($0 < x^* < L^*_{\mathrm{t}}, y^* = 0, t^* > 0$)

$$\varphi^*=0,\quad \xi^*=-\frac{\partial^2\varphi^*}{\partial y^{*2}},\quad \frac{\partial T^*}{\partial y^*}=0,\quad u^*=0,\quad v^*=0 \tag{9c}$$

and along the upper plate ($0 < x^* < L^*_{\mathrm{t}}, y^* = 1, t^* > 0$)

$$\varphi^*=1,\quad \xi^*=-\frac{\partial^2\varphi^*}{\partial y^{*2}},\quad \frac{\partial T^*}{\partial y^*}=0,\quad u^*=0,\quad v^*=0 \tag{9d}$$

where $St = fR/u_{\mathrm{o}}$ is the dimensionless pulsating frequency parameter (Strouhal number).

In addition to these, the three sets of conservation equations are coupled by the following matching conditions at the porous/solid and fluid/porous interfaces:

(4) Along the porous/solid interface (the non-slip condition, and the continuities of temperature and heat flux are accounted)

$$\begin{aligned}&u^*=0,\quad v^*=0,\quad T^*_{\mathrm{p}}\big|_{h(x,y)=0}=T^*_{\mathrm{s}}\big|_{h(x,y)=0},\\&k_{\mathrm{eff}}\frac{\partial T^*_{\mathrm{p}}}{\partial n^*}\bigg|_{h(x,y)=0}=k_{\mathrm{s}}\frac{\partial T^*_{\mathrm{s}}}{\partial n^*}\bigg|_{h(x,y)=0}\end{aligned} \tag{10}$$

(5) Along the fluid/porous interface (the continuities of the velocity, pressure, stress, temperature, and heat flux are satisfied)

$$u^*_{\mathrm{p}}\big|_{g(x,y)=0}=u^*_{\mathrm{f}}\big|_{g(x,y)=0},\quad v^*_{\mathrm{p}}\big|_{g(x,y)=0}=v^*_{\mathrm{f}}\big|_{g(x,y)=0} \tag{11a}$$

$$\begin{aligned}&\mu_{\mathrm{eff}}\frac{\partial v^*_{\mathrm{p}}}{\partial n^*}\bigg|_{g(x,y)=0}=\mu_{\mathrm{f}}\frac{\partial v^*_{\mathrm{f}}}{\partial n^*}\bigg|_{g(x,y)=0},\\&\mu_{\mathrm{eff}}\left[\frac{\partial u^*_{\mathrm{p}}}{\partial n^*}+\frac{\partial v^*_{\mathrm{p}}}{\partial\kappa^*}\right]\bigg|_{g(x,y)=0}=\mu_{\mathrm{f}}\left[\frac{\partial u^*_{\mathrm{f}}}{\partial n^*}+\frac{\partial v^*_{\mathrm{f}}}{\partial\kappa^*}\right]\bigg|_{g(x,y)=0}\end{aligned} \tag{11b}$$

$$T^*_{\mathrm{p}}\big|_{g(x,y)=0}=T^*_{\mathrm{f}}\big|_{g(x,y)=0},\quad k_{\mathrm{eff}}\frac{\partial T^*_{\mathrm{p}}}{\partial n^*}\bigg|_{g(x,y)=0}=k_{\mathrm{f}}\frac{\partial T^*_{\mathrm{f}}}{\partial n^*}\bigg|_{g(x,y)=0} \tag{11c}$$

where $g(x,y) = 0$ and $h(x,y) = 0$ are the curves defining the porous/fluid and porous/solid interfaces, and the derivative with respect to n and κ represents the normal and tangential gradients, respectively, to these curves at any point on the interfaces.

For further insight into the effects of both flow pulsation and porous cover on the heated-block heat transfer rate, the local instantaneous Nusselt number along the surfaces of the blocks is evaluated as

$$Nu_{x,t}=\frac{h_xR}{k_{\mathrm{f}}}=-\frac{k_{\mathrm{eff}}R}{k_{\mathrm{f}}(T_{\mathrm{w}}-T_{\mathrm{i}})}\frac{\partial T}{\partial y}\bigg|_{y=0}=-\frac{k_{\mathrm{eff}}}{k_{\mathrm{f}}T^*_{\mathrm{w}}}\frac{\partial T^*}{\partial n} \tag{12}$$

where $T^*_{\mathrm{w}} = (T^{\mathrm{w}} - T^{\mathrm{i}})/(q''R/k^{\mathrm{f}})$ is the dimensionless block surface temperature and n is the coordinate normal to the block surface. Then the corresponding local Nusselt number along the block surfaces in a time average over one cycle of pulsation τ is calculated as

$$Nu_x=\frac{1}{\tau}\int_0^\tau Nu_{x,t}\,\mathrm{d}t \tag{13}$$

and the cycle-space averaged overall mean Nusselt number for each heated block

$$Nu_{\mathrm{m}}=\frac{1}{\tau\Pi}\int_0^\tau\int_0^\Pi Nu_{x,t}\,\mathrm{d}x\,\mathrm{d}t \tag{14}$$

where Π is the overall exposed area of heated block. Noted that the definition of Nusselt number based on the conductivity of the fluid permits a direct comparison for a heated block with and without porous cover.

3. Numerical method and procedure

Employing a spatial non-uniform rectangular grid system, the foregoing transient finite-difference form of the vorticity transport, stream function, and energy equations were derived using control volume integration of these differential equations over discrete cells surrounding the grid points. Fig. 1(b) and (c) shows a typical non-uniform grid system employed for the present calculations. This grid system was designed to capture the steep gradients near the porous/fluid as well as porous/solid interfaces, and to provide sufficient grid density at the solid-block surfaces with minimal element distortion. In the above discretizating scheme the first-order fully implicit scheme, second-upwind-differencing, and central-differencing formats are introduced for the time derivatives, convective and diffusive terms, respectively. The transient finite difference equations thus obtained were solved by the extrapolated-Jacobi scheme. This iterative scheme is based on a double-cyclic routine, which translates into a sweep of only half of the grid points at each iteration step (Adams and Ortega [21]). In this work, convergence was considered to have been achieved when the absolute value of relative error on each grid point between two successive iterations was found to be less than 10^{-6}. In most cases, steady periodic solutions were obtained after 20–45 cycles of pulsation. The time resolution was such that one pulsating period was divided into 60 time steps during the early 5–10 cycles, and into 120 time steps for later cycles.

In addition, the harmonic mean formulation suggested by Patankar [22] was used to handle abrupt variations in thermophysical properties, such as the permeability, inertia factor, and thermal conductivity, across the interface. This ensures the continuity of the convective and diffusive fluxes across the porous/fluid interface. All of these effects on the porous/fluid interface are summarized in the dimensional parameters Reynolds number Re, Darcy number Da, Prandtl number Pr, and inertial parameter $\Lambda = \frac{F\varepsilon^2}{\sqrt{Da}}$. For the present case Re, Da, and Pr at the interface of a control volume are as follows:

$$Re_{\mathrm{I}} = \frac{2Re_{\mathrm{eff}}Re_{\mathrm{f}}}{Re_{\mathrm{eff}}+Re_{\mathrm{f}}}, \quad Da_{\mathrm{I}} = \frac{2Da_{\mathrm{eff}}Da_{\mathrm{f}}}{Da_{\mathrm{eff}}+Da_{\mathrm{f}}},$$
$$Pr_{\mathrm{I}} = \frac{2Pr_{\mathrm{eff}}Pr_{\mathrm{f}}}{Pr_{\mathrm{eff}}+Pr_{\mathrm{f}}}, \quad \Lambda_{\mathrm{I}} = \frac{2\Lambda_{\mathrm{eff}}\Lambda_{\mathrm{f}}}{\Lambda_{\mathrm{eff}}+\Lambda_{\mathrm{f}}} \tag{15}$$

where the subscripts eff, f, and I stand for effective, fluid, and interface, respectively. Therefore, instead of the source terms in Eqs. (5) and (6), the following source terms were used across the interface:

$$S^*_\varphi = \frac{u^*}{Re_{\mathrm{I}}}\frac{\partial}{\partial y^*}\left(\frac{1}{Da_{\mathrm{I}}}\right) - \frac{v^*}{Re_{\mathrm{I}}}\frac{\partial}{\partial x^*}\left(\frac{1}{Da_{\mathrm{I}}}\right) + |\overline{V}^*|u^*\frac{\partial}{\partial y^*}(\Lambda_{\mathrm{I}}) - |\overline{V}^*|v^*\frac{\partial}{\partial x^*}(\Lambda_{\mathrm{I}}) \tag{16}$$

$$S^*_\varphi = -\frac{1}{Re_{\mathrm{I}}Da_{\mathrm{I}}}\xi^* - \Lambda_{\mathrm{I}}|\overline{V}^*|\xi^* - \Lambda_{\mathrm{I}}\left[v^*\frac{\partial|\overline{V}^*|}{\partial x^*} - u^*\frac{\partial|\overline{V}^*|}{\partial y^*}\right] + \frac{u^*}{Re_{\mathrm{I}}}\frac{\partial}{\partial y^*}\left(\frac{1}{Da_{\mathrm{I}}}\right) - \frac{v^*}{Re_{\mathrm{I}}}\frac{\partial}{\partial x^*}\left(\frac{1}{Da_{\mathrm{I}}}\right) + |\overline{V}^*|u^*\frac{\partial}{\partial y^*}(\Lambda_{\mathrm{I}}) - |\overline{V}^*|v^*\frac{\partial}{\partial x^*}(\Lambda_{\mathrm{I}}) \tag{17}$$

where Eq. (16) was used for the fluid and Eq. (17) was used for the porous region. In addition, to accommodate the solution of the transport equations in both the fluid and porous regions, the effective viscosity of the fluid saturated porous medium is set to be equal to the viscosity of fluid. It had been found that this approximation provides good agreement with experimental data (Neale and Nader [23]). In this study, the computational domain was chosen to be larger than the physical domain to eliminate the entrance and exit effects and to satisfy continuity at the exit. A systematic set of numerical experiments was performed to ensure that the use of a fully developed velocity profile for the outflow boundary condition has no detectable effect on the flow solution within the physical domain.

A grid independence test showed that there is only a very small difference (less than 1%) in the time-averaged local Nusselt number distribution along the two solid block peripheral distance among the solution for (120×70), (130×90), (150×110), (180×140) and (230×180) grid distributions. Also the time step was reduced until a further reduction did not significantly affect the results on amplitude and frequency. Therefore, a 150×110 grid system was adopted for the present work. Also, special concern was paid to the grid density in the boundary layer along the solid wall. The boundary layer thickness δ/R for the classical oscillatory flow can be estimated as follows [24]:

$$\delta \sim (2\nu/\omega)^{1/2}; \quad \delta/R \sim 1/(StRe)^{1/2} \tag{18}$$

Thus the dimensionless boundary layer thickness becomes smaller as St and/or Re increases. Spatial grids were clustered to resolve the region of this thin boundary layer for high-frequent pulsation.

To validate the numerical scheme used in the present study, comparisons with three relevant results were made. This was achieved by making the necessary adjustments of our model to reduce it to a system equivalent to the simplified available cases. The relevant studies for our case correspond to the problems: (1) a steady non-pulsating forced flow in a channel with two heat solid blocks at uniform temperature, that is, $Da\to0$, and $St=0$ for $Pr=0.7$, $H^*_{\mathrm{s}}=0.25$, $S^*_{\mathrm{s}}=1.0$, $k_{\mathrm{s}}/k_{\mathrm{f}}\to\infty$, $L^*_{\mathrm{i}}=5.0$, $L^*_{\mathrm{o}}=29.0$ at $Re=500$ and 700 for $0.5\leqslant W^*_{\mathrm{s}}\leqslant3$; (2) a steady non-pulsating forced convection from a isolated heat source in a channel with a porous block attached to the upper surface wall vertically above the heating zone, (i.e., $St=0$, $H^*_{\mathrm{p}}=0.5$, $W^*_{\mathrm{p}}=1.0$ for $Re=500$, $Da=1\times10^{-2}$, $F=0.55$, $\varepsilon=0.9$, $k_{\mathrm{eff}}/k_{\mathrm{f}}=1$, $Pr=0.72$, $L^*_{\mathrm{i}}=5.5$, $L^*_{\mathrm{o}}=15$); and (3) a forced pulsating flow in a channel filled with fluid-saturated porous media, that is, $H^*_{\mathrm{p}}=1$, $W^*_{\mathrm{p}}\to\infty$. The results for the first case agree to better than 2.1% with data provided by Kim and Kang [25] for streamlines and space–space averaged overall mean Nusselt number $(Nu_{\mathrm{m}})_{\mathrm{s}}$ of each solid block for the steady non-pulsating channel flow over two heat blocks, as shown in Fig. 2(a) and (b). For the second case, the results, as shown in Fig. 2(c) and (d), are within less than 1% agreement with the data reported by Sung et al. [26] for both streamlines and isotherms. The third validity was to compare with the study of Kim et al. [12] for $Da=10^{-4}$, $Re=50$, $Pr=0.7$, $F=0.057$, $\varepsilon=0.6$, $A=0.75$, $St=0.006$ and 0.16. Comparisons between the profiles of normalized time-dependent fluctuation $u^*_{\mathrm{t\text{-}s}}=u^*_{\mathrm{t}}-u^*_{\mathrm{s}}$ of velocity u^*, where u^*_{t} is the total instantaneous velocity and u^*_{s} denotes the non-pulsating steady part, calculated in Kim et al. [12] and the current analysis show discrepancies less than 1.5%, as shown in Fig. 2(e) and (f).

4. Results and discussion

The fixed input parameters that were used for cases were $Pr=0.7$ (the air is used as the cooling fluid), $H^*_{\mathrm{s}}=0.25$, $W^*_{\mathrm{s}}=0.5$, $F=0.057$, $\varepsilon=0.6$, $R_{\mathrm{ks}}=10$, $L^*_{\mathrm{i}}=5$, and $L^*_{\mathrm{o}}=25$. In this study, emphasis is placed on the effects of Darcy number $(1\times10^{-5}\leqslant Da\leqslant1\times10^{-3})$, pulsation frequency $(0\leqslant St\leqslant1)$, pul-

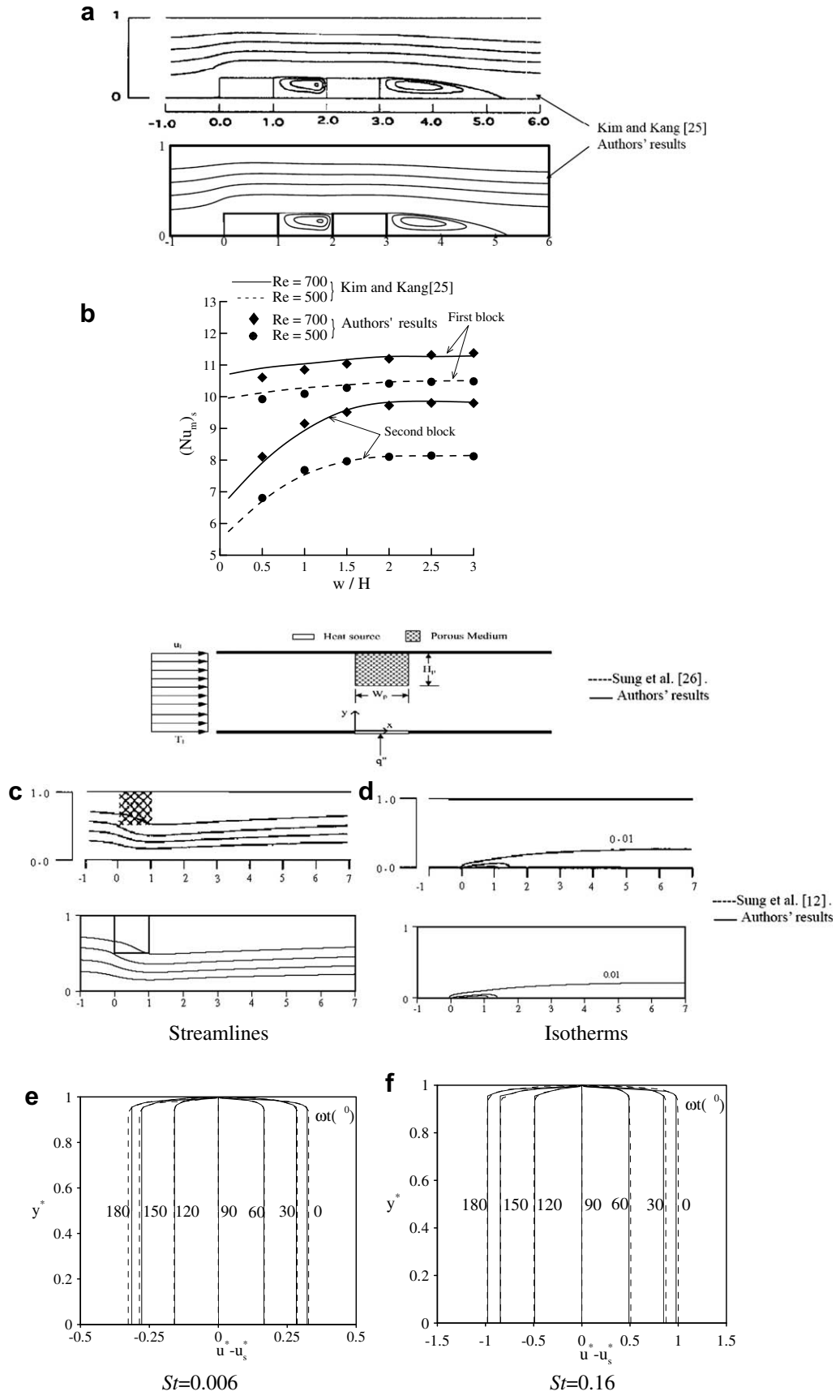

Fig. 2. The results compared with the other literatures: (a) and (b) streamlines and space-averaged Nusselt number $(Nu_m)_s$ for the steady non-pulsating flow compared with Kim and Kang [25], (c) and (d) streamlines and isotherms compared with Sung et al. [26], and (e) and (f) profiles of time-dependent fluctuation of u^* compared with Kim et al. [12] for St = 0.006 and 0.16, respectively.

Table 1
Input data of governing parameters for a porous-covering heated blocks array

Case	Da	A	St	H_p^*	W_p^*	S_s^*	R_{keff}	N_s
1	1×10^{-3}	0.4	0.6	0.3	1.0	1.0	1.0	2
	1×10^{-4}	0.4	0.6	0.3	1.0	1.0	1.0	2
	3×10^{-5}	0.4	0.6	0.3	1.0	1.0	1.0	2
2	5×10^{-5}	0.2	0.6	0.3	1.0	1.0	1.0	2
	5×10^{-5}	0.4	0.6	0.3	1.0	1.0	1.0	2
	5×10^{-5}	0.6	0.6	0.3	1.0	1.0	1.0	2
3	5×10^{-5}	0.4	0.1	0.3	1.0	1.0	1.0	2
	5×10^{-5}	0.4	0.4	0.3	1.0	1.0	1.0	2
	5×10^{-5}	0.4	0.7	0.3	1.0	1.0	1.0	2
4	5×10^{-5}	0.4	0.6	0.3	1.0	1.0	1.0	2
	5×10^{-5}	0.4	0.6	0.375	1.0	1.0	1.0	2
	5×10^{-5}	0.4	0.6	0.4	1.0	1.0	1.0	2
5	5×10^{-5}	0.4	0.6	0.3	0.8	1.0	1.0	2
	5×10^{-5}	0.4	0.6	0.3	1.0	1.0	1.0	2
	5×10^{-5}	0.4	0.6	0.3	1.2	1.0	1.0	2
6	5×10^{-5}	0.4	0.6	0.3	1.0	0.8	1.0	2
	5×10^{-5}	0.4	0.6	0.3	1.0	1.2	1.0	2
	5×10^{-5}	0.4	0.6	0.3	1.0	1.4	1.0	2
7	5×10^{-5}	0.4	0.6	0.3	1.0	1.0	1.0	2
	5×10^{-5}	0.4	0.6	0.3	1.0	1.0	10	2
	5×10^{-5}	0.4	0.6	0.3	1.0	1.0	100	2
8	5×10^{-5}	0.4	0.6	0.3	1.0	1.0	1.0	1
	5×10^{-5}	0.4	0.6	0.3	1.0	1.0	1.0	3
	5×10^{-5}	0.4	0.6	0.3	1.0	1.0	1.0	5

sation amplitude ($0 \leqslant A \leqslant 0.8$), geometric parameters ($0.3 \leqslant H_p^* \leqslant 0.4, 0.8 \leqslant W_p^* \leqslant 1.2, 0.8 \leqslant S_s^* \leqslant 1.4$), and the effective conductivity ratio ($1 \leqslant R_{keff} \leqslant 100$) on the flow and heat transfer characteristics. Table 1 displays various parameter set considered in this analysis. The parameter sets presented in Table 1 were only a subset of much larger set that was investigated in this work. The parameter sets introduced in Table 1 were found to be most important in revealing aspects of the geometric arrangements of the porous cover and variations in the flow pulsation. Figs. 5–12 show time-dependent streamlines and cycle-average local Nusselt number distribution over porous-covering blocks array for the corresponding cases listed in Table 1. To illustrate the results of flow and temperature fields near the porous-covering heated blocks clearly, only this region and its vicinity are presented. However, it should be noted that the computational domain included a much larger region than what is displayed in the subsequent figures. Furthermore, for the sake of brevity, only the main features and characteristics of some of the results are discussed and the corresponding figures are not presented.

4.1. Steady flow

For comparison purpose, the typical velocity and temperature fields around the porous-covering heated blocks in the case of a steady non-pulsating flow ($St = 0$) are displayed in Fig. 3 for $L_i^* = 5$, $L_o^* = 25$, $Re = 250$, $S_s^* = 1.0$, $H_s^* = 0.25$, $W_s^* = 0.5$, $H_p^* = 0.3$, $W_p^* = 1.0$, $R_{keff} = 1$, $R_{ks} = 10$ at $Da = 1\times10^{-2}$, 1×10^{-3}, 1×10^{-4}, 7×10^{-5}, 5×10^{-5}, 3×10^{-5}, and 1×10^{-5}, respectively. It can be observed from Fig. 3(a) that the streamlines are considerably distorted in the channel due to the presence of the porous-covering block array. As Darcy number decreases from 1×10^{-2} to 1×10^{-5}, the distortion of streamlines and the size of recirculations behind the blocks become more pronounced. At the smaller Darcy number, the core flow creates four vortex effects, when it interacts with the porous-covering two-block array: a weak recirculation zone ahead of the first block, a clockwise (CW) recirculation between solid blocks, a relatively strong recirculation behind the last block, and a large counterclockwise (CCW) eddy zone on the smooth upper plate surface corresponding to the reattached region on the bottom plate. The variation of these complicated flow field within the channel is the consolidated result of the following four effects: (1) a penetrating effect pertaining to the porous medium, (2) a blowing effect caused by porous media displacing transversely the fluid from the porous region into the fluid region, (3) a suction effect caused by the pressure drop behind the porous-covering blocks resulting in a reattached flow, and (4) the effects of boundary-layer separation. It should be noted that within the interblock cavity, the streamlines between the recirculation center and the upstream wall (CD) of that cavity are slightly denser than those between the recirculation center and the downstream wall (EF) of the cavity. This shows that the magnitude of upward velocity near the upstream cavity wall (CD) is slightly larger than that of the downward velocity near the downstream wall (EF), which may transport more convective energy from the upstream wall (CD) than the downstream wall (EF) of cavity. Fig. 3(b) shows the isotherms corresponding to the above flow field. The thermal boundary layer thickness increases over the two porous-covering block array, and decreases downstream from the block array. Here, the distortion of isotherms arises partly due to the variation in the cross-sectional area of core flow and partly the displacement of fluid from the porous region into the fluid region occurring at the top face of each block. The level of isotherms distortion increases with decreasing Da number. At smaller Darcy number, within the interblock space spacing between isotherms is closer in the upstream end (CD) than in the downstream end (EF). This indicates that a higher temperature gradient in the right face (CD) of block than in the left face (EF) of proceeding block.

The local Nusselt number distributions around the exposed faces of the two heated blocks for this case are depicted in Fig. 3(c). At larger Darcy number ($Da = 1\times10^{-2}$), along the left face (AB) of first block, Nu_x is small at the lower corner (point A) and it grows as the reattachment point is approached due to the recirculation effect. The maximum Nu_x occurs at the upper corner (point B). For the top face (BC) of first block, the Nu_x is largest at the left corner and then decreases rapidly to a local minimum value. Near the (block top) right corner (point C) Nu_x increases slightly. This can be explained by noting that since this surface is parallel to the flow direction, as the fluid turns around the corner, a thermal boundary layer starts to develop at the left corner (point B). Under the blowing effect caused by porous matrix attached to that surface, the thickness of thermal boundary layer grows up quickly. Downstream the top face (BC), the boundary-layer separation occurs, resulting in an increase in the convective energy transport again due to the fluid mixing. On the block right face (CD), Nu_x is large at the upper corner (point C) and decreases rapidly to a small, nearly constant value before rising at the bottom corner (point D) where the temperature is greater. For the left, top, and right faces in the two-heated block array, Nu_x decreases with downstream blocks. The reason is that as the fluid passed over first block, the temperature of the fluid increases. Consequently, the temperature difference between the fluid and the block decreases as the fluid moves downstream; as a result, the local Nusselt number decreases progressively with downstream blocks.

Fig. 3(c) displays also how Nu_x distributions around the two heated block exposed surfaces changes with Darcy number. In the range of $1\times10^{-2} \geqslant Da \geqslant 3\times10^{-5}$ for the first block, Nu_x decreases along the left face (AB) as Da decreases because of the smaller impact of core flow on the left face (AB). Along its top faces (BC), as Da decreases, the decreasing tendency of local Nusselt number distribution from a local maximum value at the left corner (point B) to a local minimum value near the right corner (point C) is steeper. This phenomenon is due to the fact that a smaller value of Da translates into larger blowing effects, which in turn increases the increment of thermal boundary layer thickness. The maximum value of Nu_x occurring at the leading edge (point B) of top face (BC)

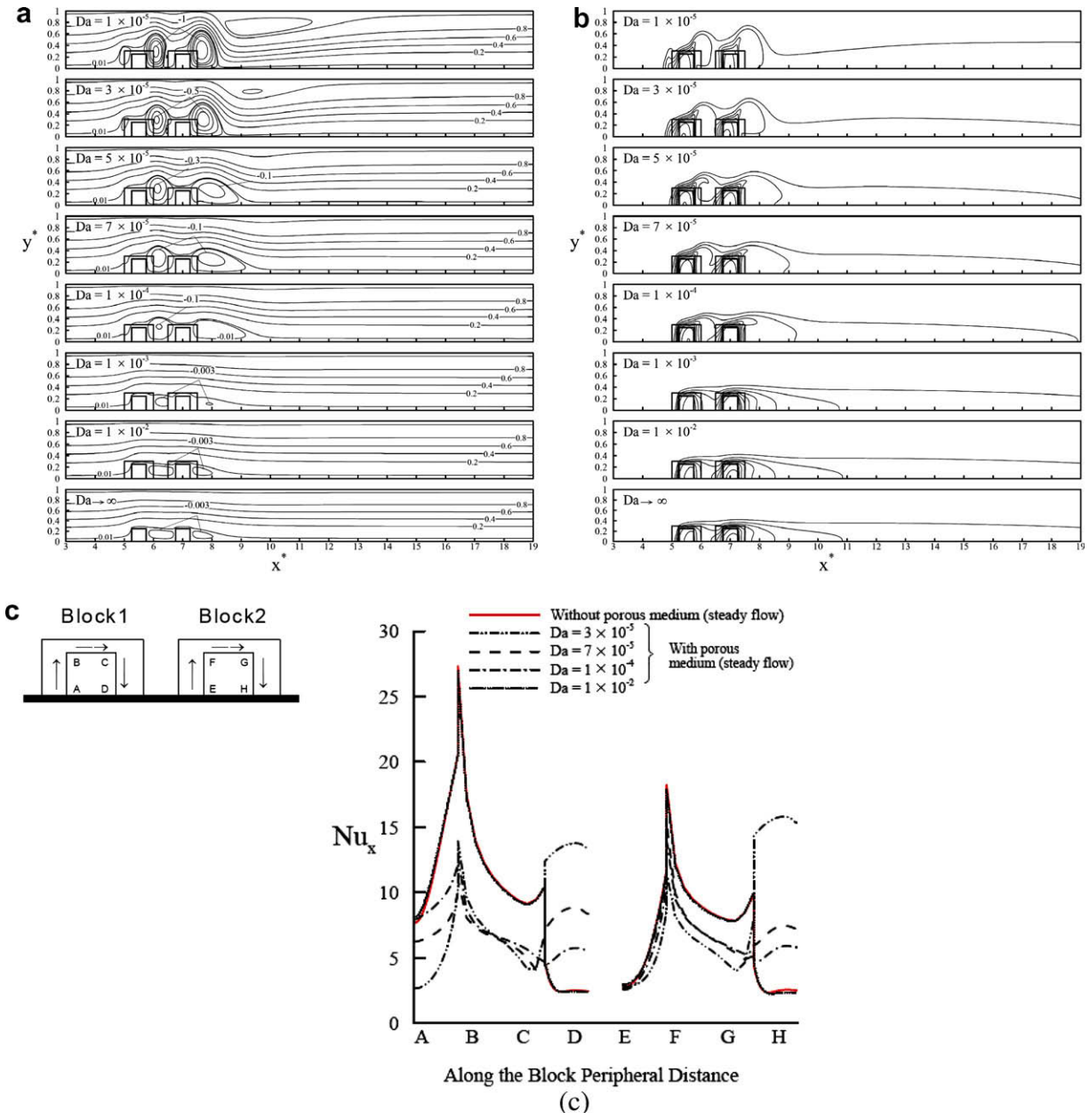

Fig. 3. Effects of the Darcy number on (a) streamlines ($\Delta\varphi^* = 0.2$ for $0 < \varphi^* < 1$) and (b) isotherms ($\Delta T^* = 0.1$ for $0 < \Delta T^* < 1$), and (c) local Nusselt number distribution for a steady non-pulsating flow.

increases with decreasing *Da* due to the larger temperature gradient caused by the larger recirculation flow ahead of the first block. Near the top right corner (point C), Nu_x decreases to a local minimum value and then increase slightly. This increased level becomes more significant for smaller *Da* due to the stronger separation flow downstream the top faces (BC). Whereas, along its right face (CD), Nu_x increases with decreasing *Da* due to the larger recirculation behind it, which can convect more thermal energy away from the block. For the right faces (GH) of second blocks, Nu_x increases with decreasing *Da* due to the stronger interaction between the core flow and the downstream recirculation flow. Along its top (FG) and left (EF) faces Nu_x decreases as *Da* decreases because of the smaller interaction between the interblock recirculating zone with the left face (EF) and the smaller temperature gradient at the leading-edge corner of the top face (FG). Comparison of local Nusselt number distributions for the two-block array with and without porous cover ($Da \to \infty$) shows that the extension-transverse recirculating flow caused by porous medium can augment significantly the heat transfer rate from the block right faces (CD or GH) to the core flow by convection, as discussed previously. More other relative parametric effects on the steady flow field and heat transfer can be found on reference [8].

4.2. Pulsating flow

The above-stated steady and stable flow field can be destabilized by inducing pulsation, which leads to better flow mixing and further enhanced thermal transport. The influence of external forced pulsation on the flow and temperature fields is now investigated. Fig. 4(a) and (b) portraits the flow patterns and thermal fields over one pulsating cycle at a periodic-steady state with eight successive phase angle of $\omega t = 0$, $\pi/4$, $\pi/2$, $3\pi/4$, π, $5\pi/4$, $3\pi/2$, and $7\pi/4$ for $Re = 250$, $St = 0.6$, $A = 0.4$, $W_p^* = 1.0$, $H_p^* = 0.3$, and $R_{keff} = 1.0$ at $Da = 5 \times 10^{-5}$. In Fig. 4(c) the u^* is plotted as a function

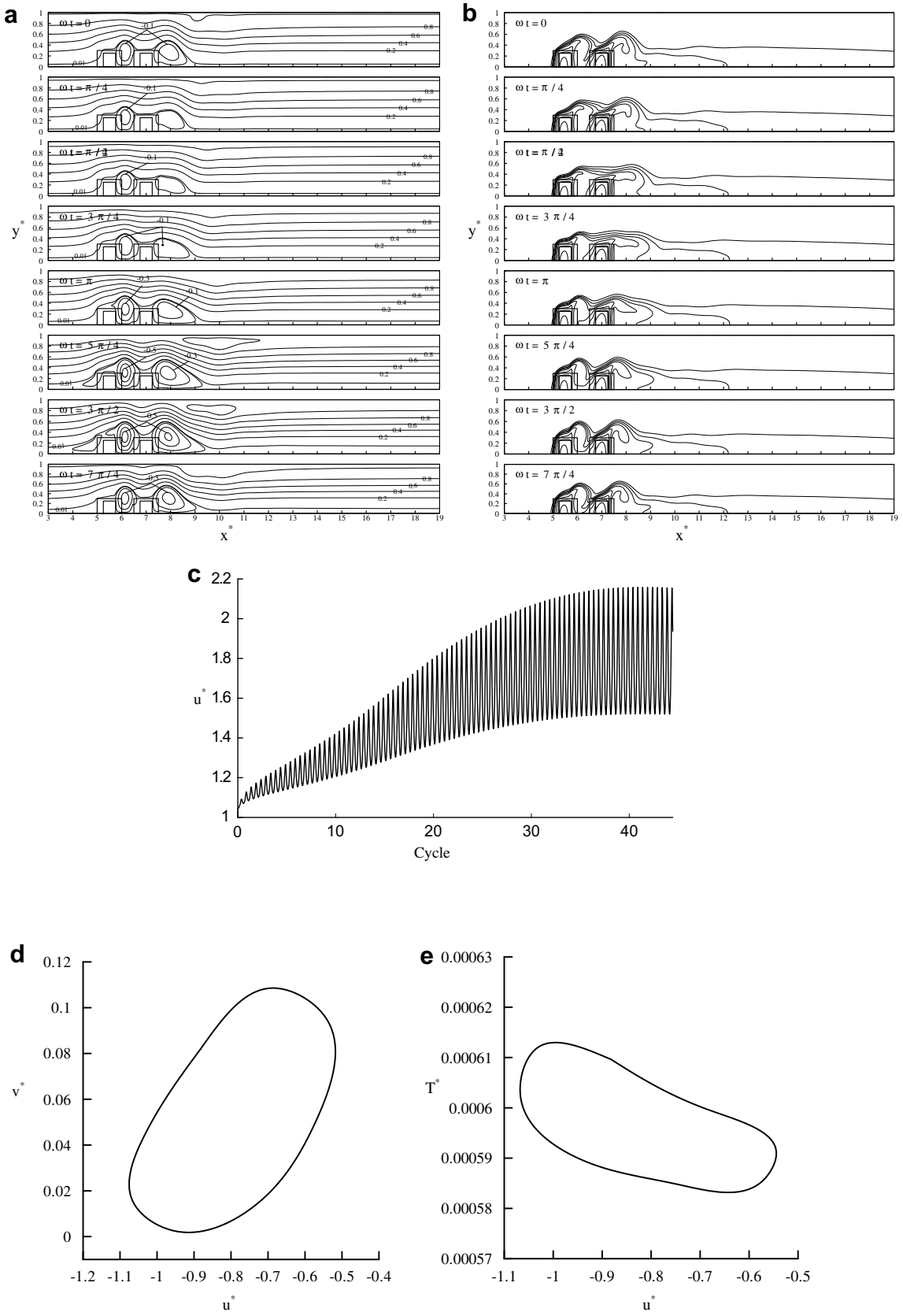

Fig. 4. The variations of (a) streamlines ($\Delta\varphi^* = 0.2$ for $0 < \varphi^* < 1$), (b) isotherms ($\Delta T^* = 0.1$ for $0 < \Delta T^* < 1$), (c) u^* vs. t, (d) phase diagram of u^* vs. v^*, and (e) u^* vs. T^* at $(x^*, y^*) = (L_i^* + W_p^*/2, H_p^*/2)$ during a periodic-steady cycle.

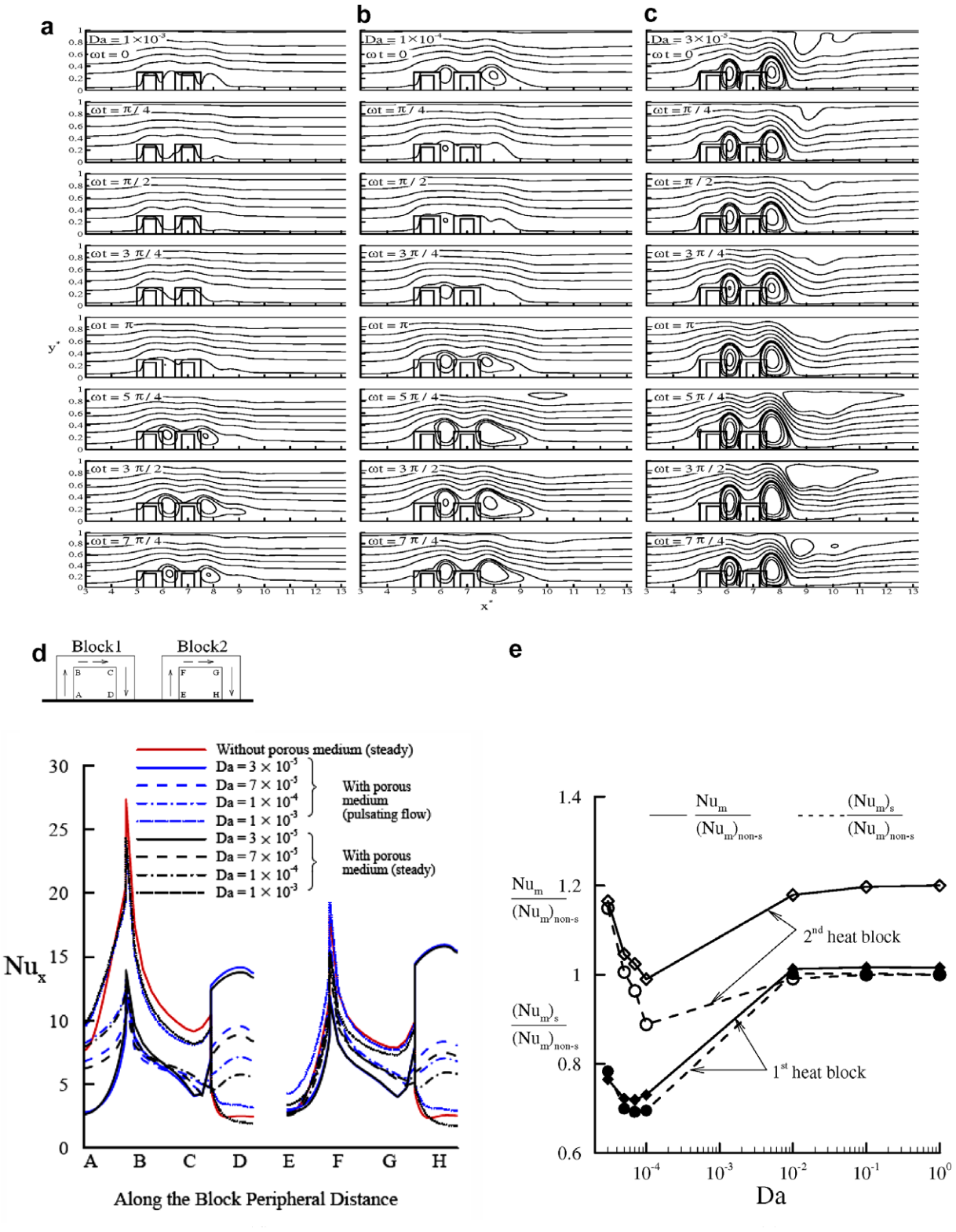

Fig. 5. Effects of the Darcy number on the variations of streamlines ($\Delta\varphi^* = 0.2$ for $0 < \varphi^* < 1$) (a)–(c), cycle-averaged local Nusselt number (d), and heat transfer enhancement factor (e) during a periodic-steady cycle.

of time at a monitoring point $(x = L_i^* + W_p^* + S_p^*/2, y = H_p^*/2)$ for the case with $Da = 5 \times 10^{-5}$. The x-component velocity u^* exhibits a time-asymptotic periodic-steady behavior after about 40 cycles of pulsation. Fig. 4(d) and (e) shows phase diagrams of v^* vs. u^* and T^* vs. u^* at the same monitoring point. These phase diagrams display a simple closed loop, which clearly indicate that the flow and thermal fields are in a high time-periodic regime. The same well-closed loops are also found for other cases of Darcy numbers. It can be seen from Fig. 4(a) the previously-mentioned four recirculating cells, caused by porous-covering blocks, shrink and expand

cyclically under the action of external forcing pulsation. Each instantaneous flow pattern is the overall results of four competing effects of penetrating, blowing, suction and boundary layer separation as mentioned earlier. This periodic alternation of flow structure contributes to the bulk mixing of fluids in the porous-covering block region, especially in inter-block and downstream recirculation zones. The oscillating interaction of recirculations, caused by both porous block and forced Pulsation, with the core flow influences significantly the heat transfer rate from each heated block faces. Fig. 4(b) shows the impact of pulsation on the thermal field. Comparison of Fig. 4(b) with Fig. 3(b) indicates that the thermal field under a pulsating flow presents a periodic oscillation of the isotherm field. The thermal boundary layer thickness along the block surfaces descends during the acceleration phase of the cycle ($\omega t = 0$ to $\pi/2$ and $3\pi/2$ to 2π), and rises during the deceleration phase of the cycle ($\omega t = \pi/2$ to $3\pi/2$). This is because when the flow velocity is low, the ratio of fluid residence time over the heated block surfaces to the heat diffusion time is high, allowing more heat to diffuse per unit volumetric flow. This leads to higher flow temperatures and less steep temperature gradient at the wall. The depth of heat penetration into the fluid increases at those times. When the flow velocity is high, decreasing that ratio leads to lower flow temperatures and greater temperature gradients.

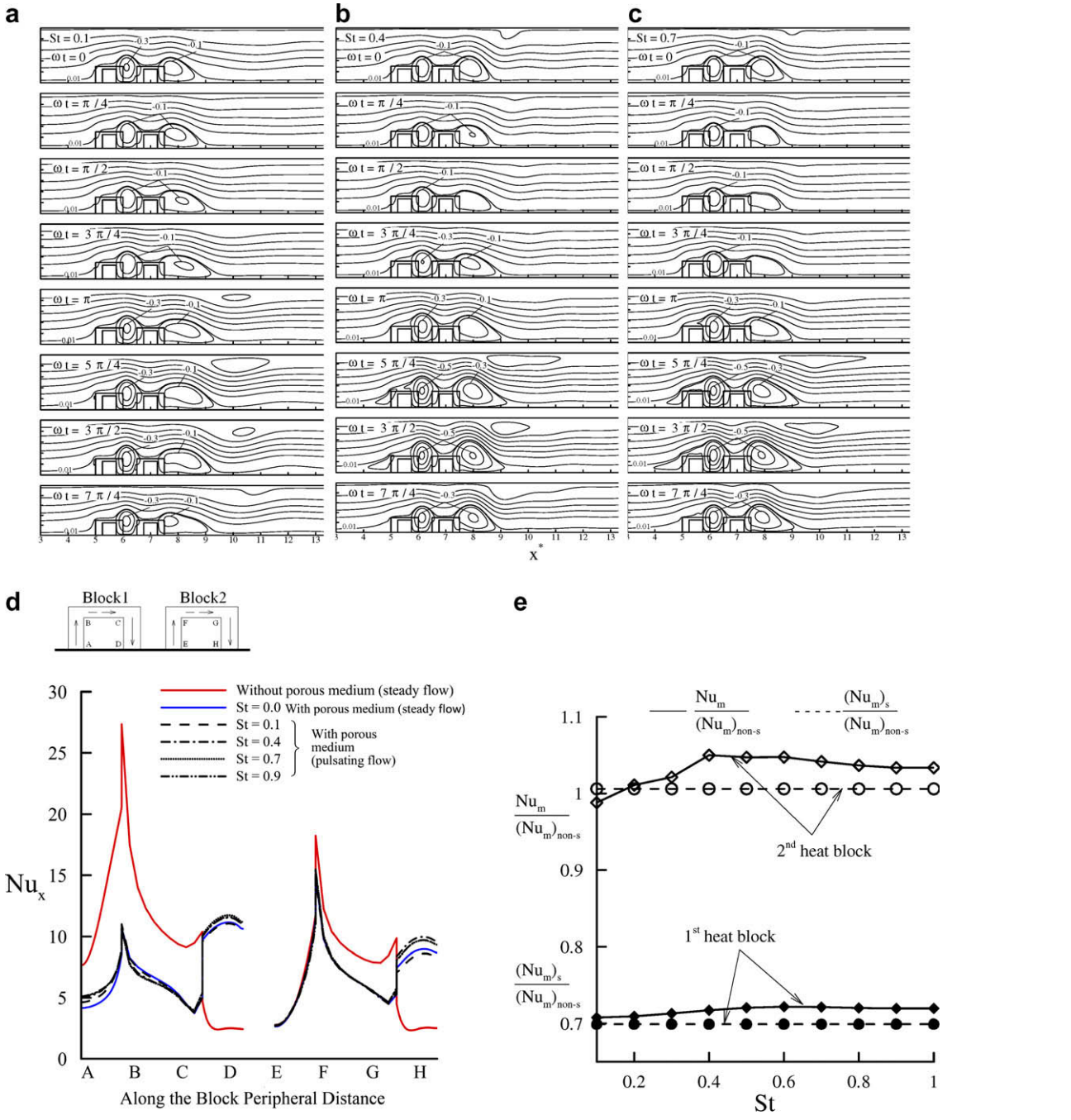

Fig. 6. Effects of the pulsating amplitude on the variations of streamlines ($\Delta\varphi^* = 0.2$ for $0 < \varphi^* < 1$) (a)–(c), cycle-averaged local Nusselt number (d), and heat transfer enhancement factor (e) during a periodic-steady cycle.

4.3. Effect of Darcy number Da

To investigate the effect of Darcy number on the pulsating flow and temperature fields, computations were carried out at $Da = 1 \times 10^{-3}$, 1×10^{-4}, and 3×10^{-5}, respectively, for $Re = 250$, $St = 0.6$, $A = 0.4$, $W_p^* = 1.0$, $H_p^* = 0.3$, and $R_{keff} = 1.0$. Comparison of the streamline variation in Fig. 5(a)–(c) shows that as the Darcy number increases from 3×10^{-5} to 1×10^{-3}, the distortions of instantaneous streamlines become less pronounced, and the CCW eddy zone on the smooth upper plate becomes smaller and finally disappears at each time instant. This is due to the smaller bulk frictional resistance that the flow encounters in the porous region at larger values of Darcy number, which in turn accelerates the core flow through the porous-covering blocks and confines the development of recirculation zones in the transverse direction. The pulsating temperature fields are affected in a similar way. Fig. 5(d) shows the variation of cycle-averaged local Nusselt number Nu_x along the solid block surfaces with *Da*. For the case of pulsation flow with porous block, the variation tendency of Nu_x vs. *Da* is the same as that in the stated-previously case of steady non-pulsation flow with porous-covering heat sink. But, as expected, the values of Nu_x for pulsating-flow case are higher than that for the steady-flow case.

In order to obtain an overall measure of heat transport characteristics in the present study, the influence of both flow pulsation and porous-covering heat sink on the heat transfer enhancement

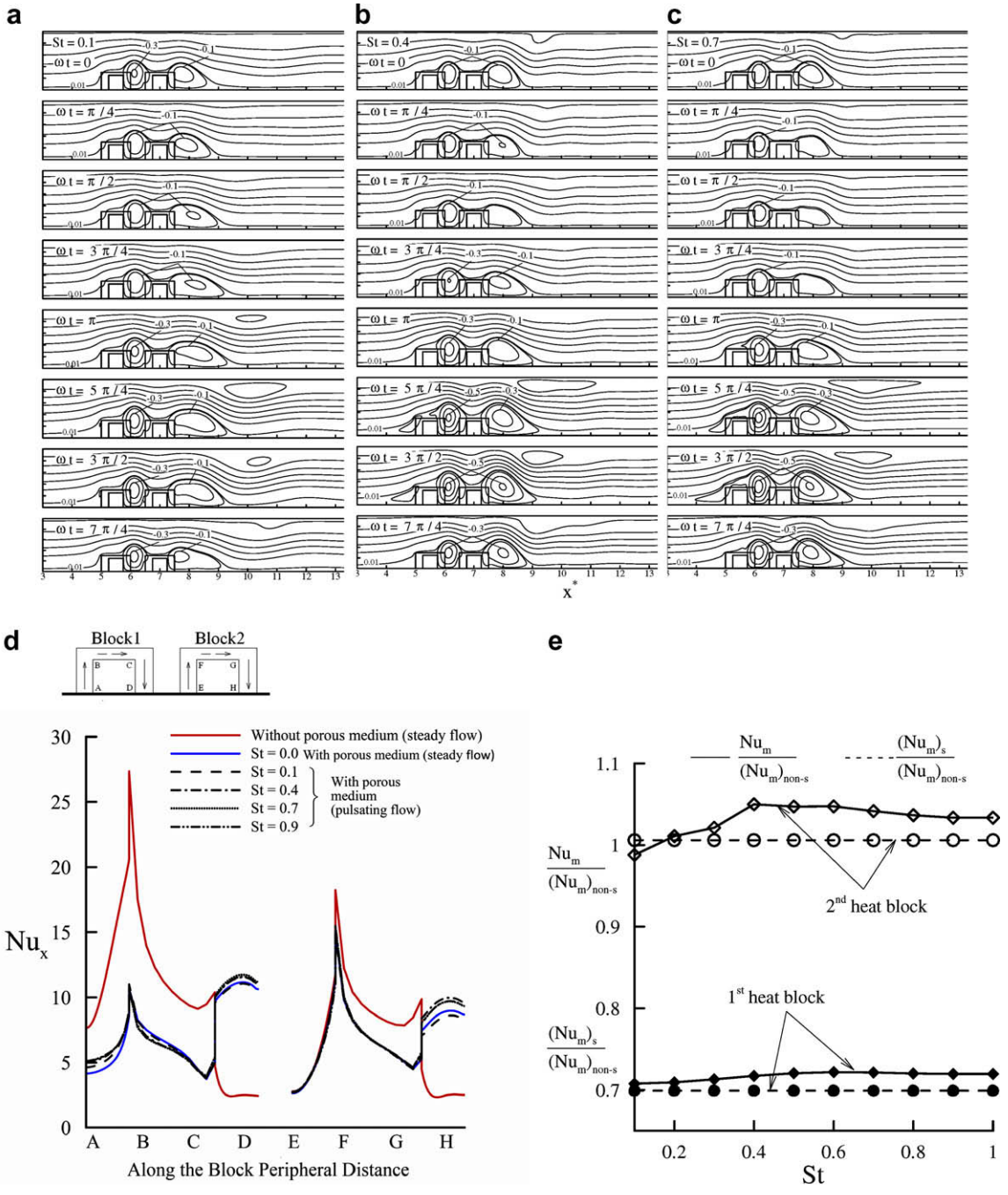

Fig. 7. Effects of the Strouhal number on the variations of streamlines ($\Delta\varphi^* = 0.2$ for $0 < \varphi^* < 1$) (a)–(c), cycle-averaged local Nusselt number (d), and heat transfer enhancement factor (e) during a periodic-steady cycle.

factors $Nu_m/(Nu_m)_{non\text{-}s}$ and $(Nu_m)_s/(Nu_m)_{non\text{-}s}$, which give the cycle-space averaged overall mean Nusselt number Nu_m and steady space-averaged overall mean Nusselt number $(Nu_m)_s$ over a heated block normalized by the corresponding steady non-pulsation non-porous-covering value $(Nu_m)_{non\text{-}s}$, is calculated. Fig. 5(e) exhibits the effect of Da on $Nu_m/(Nu_m)_{non\text{-}s}$ and $(Nu_m)_s/(Nu_m)_{non\text{-}s}$. Here, abscissa is expressed in log scale to show clearly the effect of Da in the range of $1–1 \times 10^{-5}$. It is clear from Fig. 5(e) that in the calculation range of Da, there exists a critcal Darcy number (about $Da = 1 \times 10^{-4}$) corresponding to the smallest values of $Nu_m/(Nu_m)_{non\text{-}s}$ and $(Nu_m)_s/(Nu_m)_{non\text{-}s}$, beyond or below which both heat transfer enhancement factors increase. For the case of steady flow with porous cover, the heat transfer rate is enhanced ($(Nu_m)_s/(Nu_m)_{non\text{-}s} > 1$) for the second heated block at smaller Da ($< 3 \times 10^{-5}$) due to increased convection aided by higher velocities in the downstream recirculation eddy (see Fig. 3(c)). This enhanced effect on the second block heater is better than that on the first one. For larger Da($> 4 \times 10^{-5}$), the heat transfer rate is lessened ($(Nu_m)_s/(Nu_m)_{non\text{-}s} < 1$) for both heated blocks due to the reduction of the mass flow rate passing over the surface of block heater comparing with the case without porous cover. For the case of pulsating flow with porous cover, the value of pulsating heat transfer enhancement factor $Nu_m/(Nu_m)_{non\text{-}s}$ is higher than that of steady heat transfer enhancement factor $(Nu_m)_s/(Nu_m)_{non\text{-}s}$ due to the

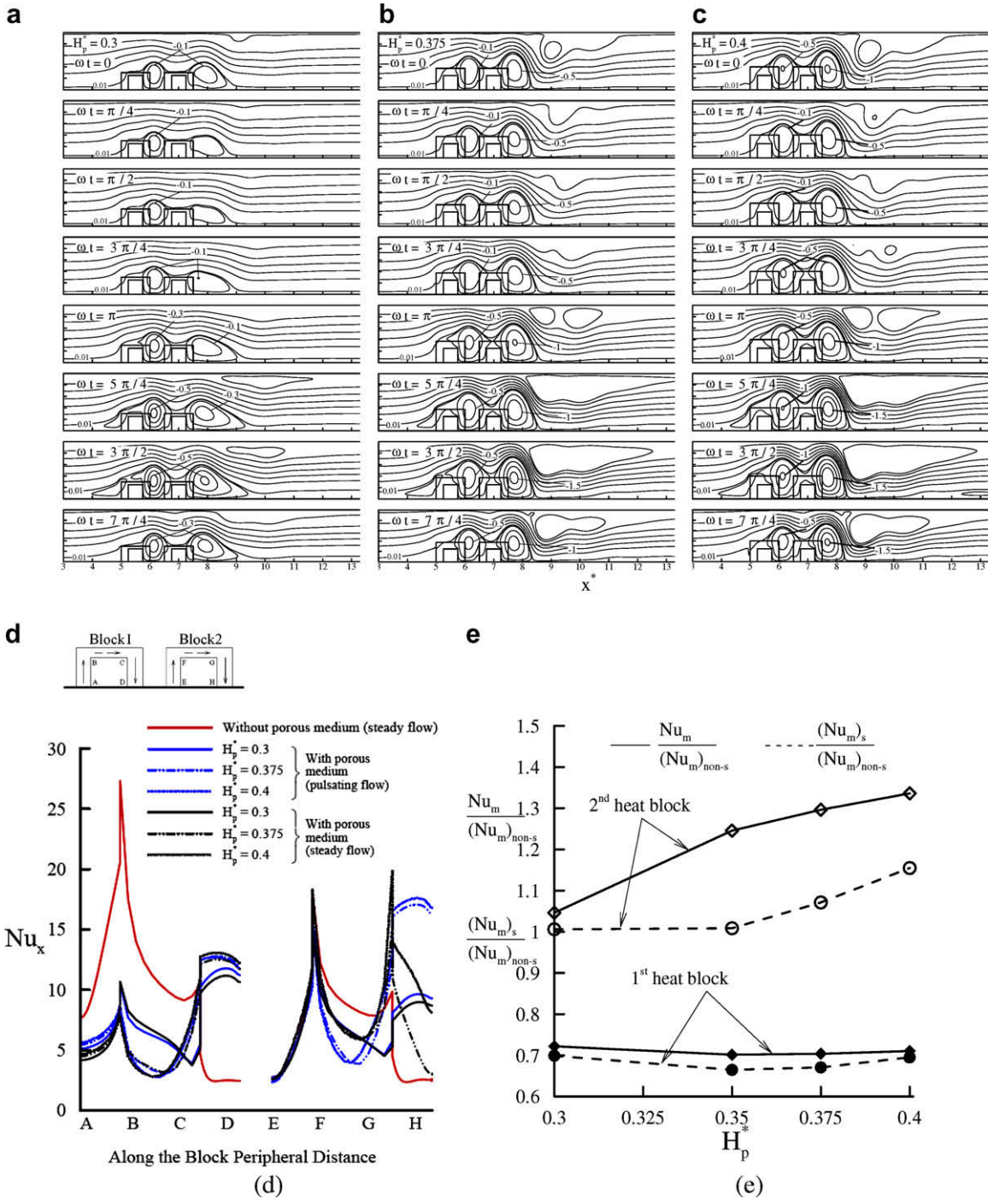

Fig. 8. Effects of the porous-covering geometric parameters H_p^* on the variations of streamlines ($\Delta\varphi^* = 0.2$ for $0 < \varphi^* < 1$) (a)–(c), cycle-averaged local Nusselt number (d), and heat transfer enhancement factor (e) during a periodic-steady cycle.

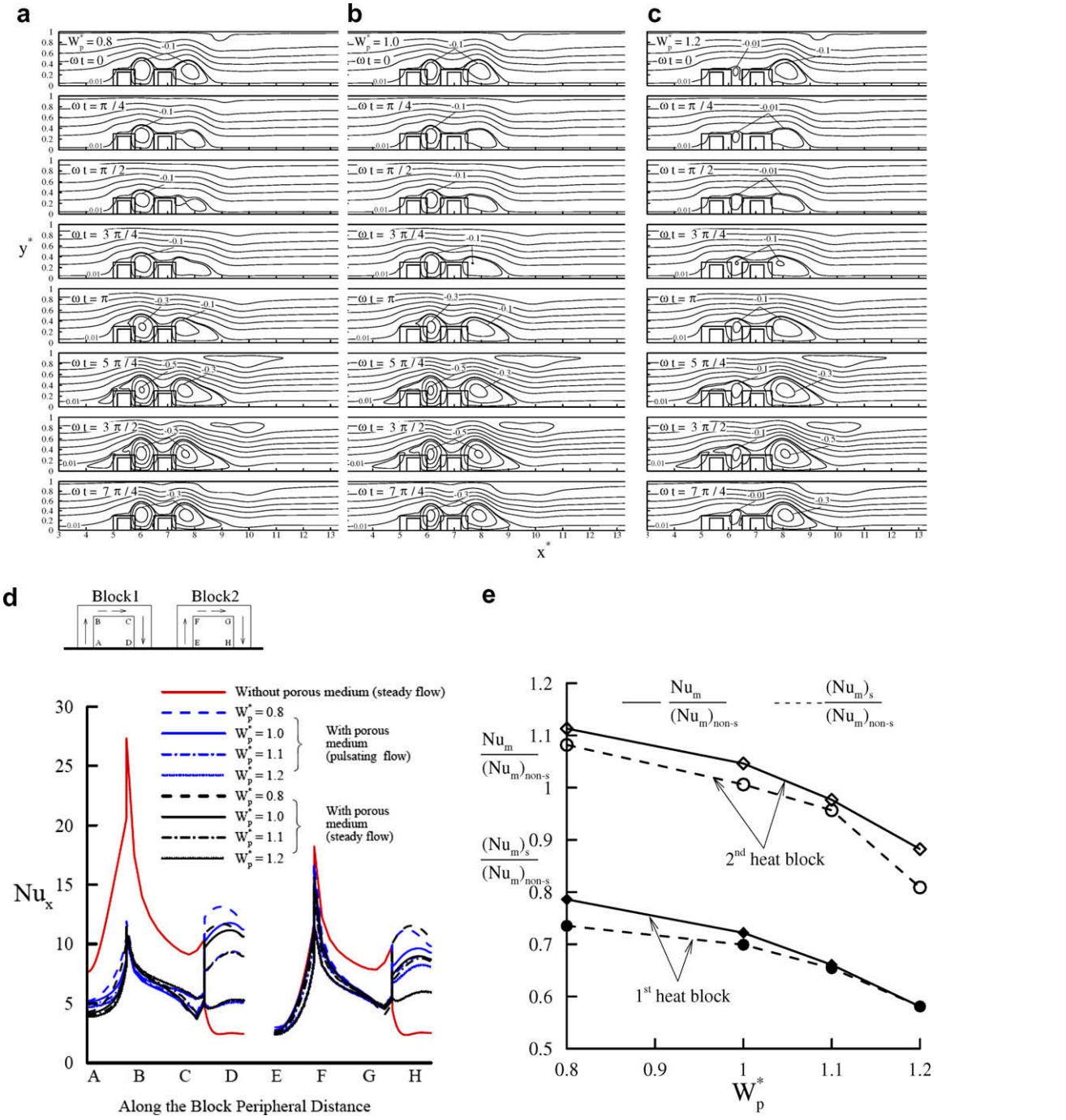

Fig. 9. Effects of the porous-covering geometric parameters W_p^* on the variations of streamlines ($\Delta\varphi^* = 0.2$ for $0 < \varphi^* < 1$) (a)–(c), cycle-averaged local Nusselt number (d), and heat transfer enhancement factor (e) during a periodic-steady cycle.

larger cycle-space averaged temperature gradient near the heated block surfaces. The second heater has larger value of $Nu_m/(Nu_m)_{non\text{-}s}$ than the first heater. For second heater, when $Da=2\times10^{-5}$, the cycle-space average overall mean Nusselt number of pulsating flow is about 1.18 times that of non-pulsating flow and about 1.02 times that of non-pulsating flow over nonporous-covering heater. Noted that when $1 > Da > 1\times10^{-2}$, $Nu_m/(Nu_m)_{non\text{-}s} = 1.2$. This enhanced heat transfer is due to the periodic burst of recirculating cells in the inter-block region and in the downstream region of the second block (see Fig. 4(a)), which enhanced the interaction between the groove or back-facing step of the two solid block array and the mainstream flow. The higher cycle-space averaged Nusselt number ($Nu_m/(Nu_m)_{non\text{-}s} > 1$) indicates that the porous-covering block heater subjected to pulsating flow has a higher heat dissipation rate compared to steady flow.

4.4. Effect of the pulsating amplitude A

The influence of pulsating amplitude A on the flow and temperature fields over a periodic-steady pulsating cycle is shown in Fig. 6. for $Re = 250$, $Da=5\times10^{-5}$, $St = 0.6$, $S_s^* = 1.0$, $H_s^* = 0.25$, $W_s^* = 0.5$, $H_p^* = 0.3$, $W_p^* = 1.0$, and $R_{keff} = 1.0$ at $A = 0.2$, 0.4, and 0.6, respectively. Based on the inlet pulsating velocity in Eq. (9a), the larger the pulsating amplitude A is, the higher the flow decel-

eration becomes during the flow pulsation reversal ($\omega t = \pi$ to 2π), which leads to the produce of the stronger recirculation zones. The reason for this trend is that increasing A decreases the fluid's forward momentum, resulting in a smaller penetration into the porous matrix. This, in turn, increases the action of the blowing effect caused by porous medium on the block top face and enhances the expansion of recirculation flows in the transverse direction. In addition, as A increases the area of downstream vortex zone attaching on the upper plate extends axially and the size of the weak vortex zone ahead of the first block increases. As expected, the distortion of temporal isotherms in the channel region corresponding to the flow field becomes more pronounced with an increase in A. Fig. 6(d) displays the effect of A on the variation of Nu_x around the two block faces. For each block top faces, the temporal heat transfer rate from the top faces slightly decreases as the pulsating amplitude increases. This is due to the smaller instantaneous velocities near the top face for larger pulsating amplitude, which convects lower thermal energy away from the face. Along

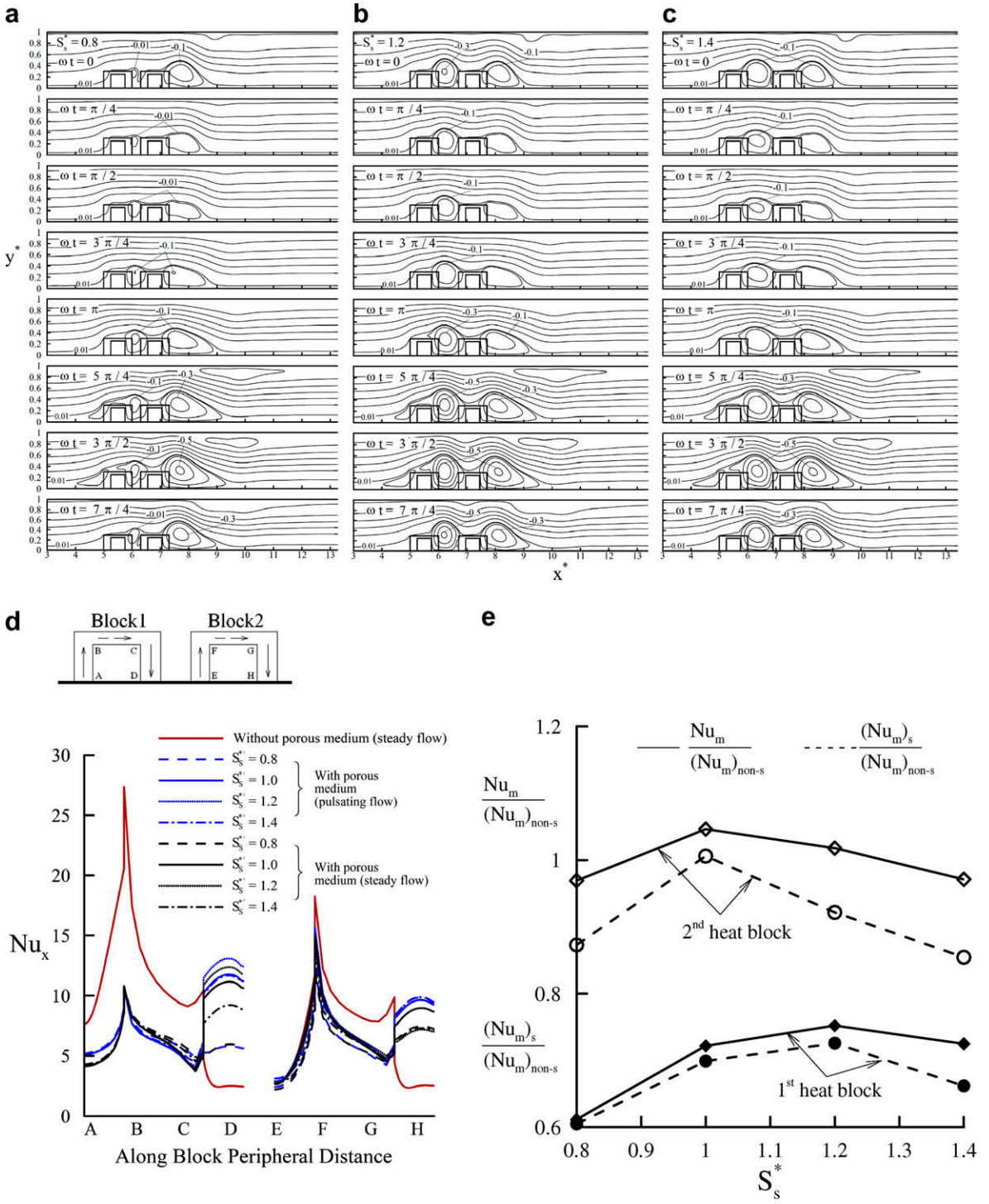

Fig. 10. Effects of the porous-covering geometric parameters S_s^* on the variations of streamlines ($\Delta\varphi^* = 0.2$ for $0 < \varphi^* < 1$) (a)–(c), cycle-averaged local Nusselt number (d), and heat transfer enhancement factor (e) during a periodic-steady cycle.

the left and right faces, for larger A the first block has much larger Nu_x values along its left face because of the larger impact of core flow as it turns upwards and accelerates into the bypass region. The last block has also larger Nu_x value along its right face because of the larger oscillation temperature difference between the fluid and the block as the fluid moves downstream. The remaining vertical faces within the two-block array, the Nu_x slightly increases along the second block right face and increases along the first block left face as A increases from 0.2 to 0.8. The thermal transport from these faces is dominated by the interblock recircuation. The larger the value of A, the stronger the temporal recirculation zone, which enhances convective heat transfer from these block faces. Fig. 6(e) gives the results for cycle-space average overall block mean Nusslt numbers. It can be seen that as A increases the gain in $Nu_m/(Nu_m)_{non\text{-}s}$ increases. The second heated block has a larger heat transfer enhancement factors $Nu_m/(Nu_m)_{non\text{-}s}$ and $(Nu_m)_s/(Nu_m)_{non\text{-}s}$ than the first one.

4.5. Effect of the pulsating frequency St

The effect of variations in the pulsating frequency or Strouhal number is depicted in Fig. 7 for $Re = 250$, $Da = 5 \times 10^{-5}$, $A = 0.4$, $S_s^* = 1.0$, $H_s^* = 0.25$, $W_s^* = 0.5$, $H_p^* = 0.3$, $W_p^* = 1.0$, and $R_{keff} = 1$, with $St = 0.1$–1.0. The flow fields during a pulsating cycle with a phase angle increment of $\pi/4$ reveal that as St increases from 0.1 to 0.4, the size of all the recirculation zones in the channel slightly increases in the longitude direction (as shown in Fig. 7(a) and (b)), and reduces as St is increased further to 0.7. As expected, the instantaneous thickness of thermal boundary layers along the block surfaces decreases with the increase of St from 0.1 to 0.4,

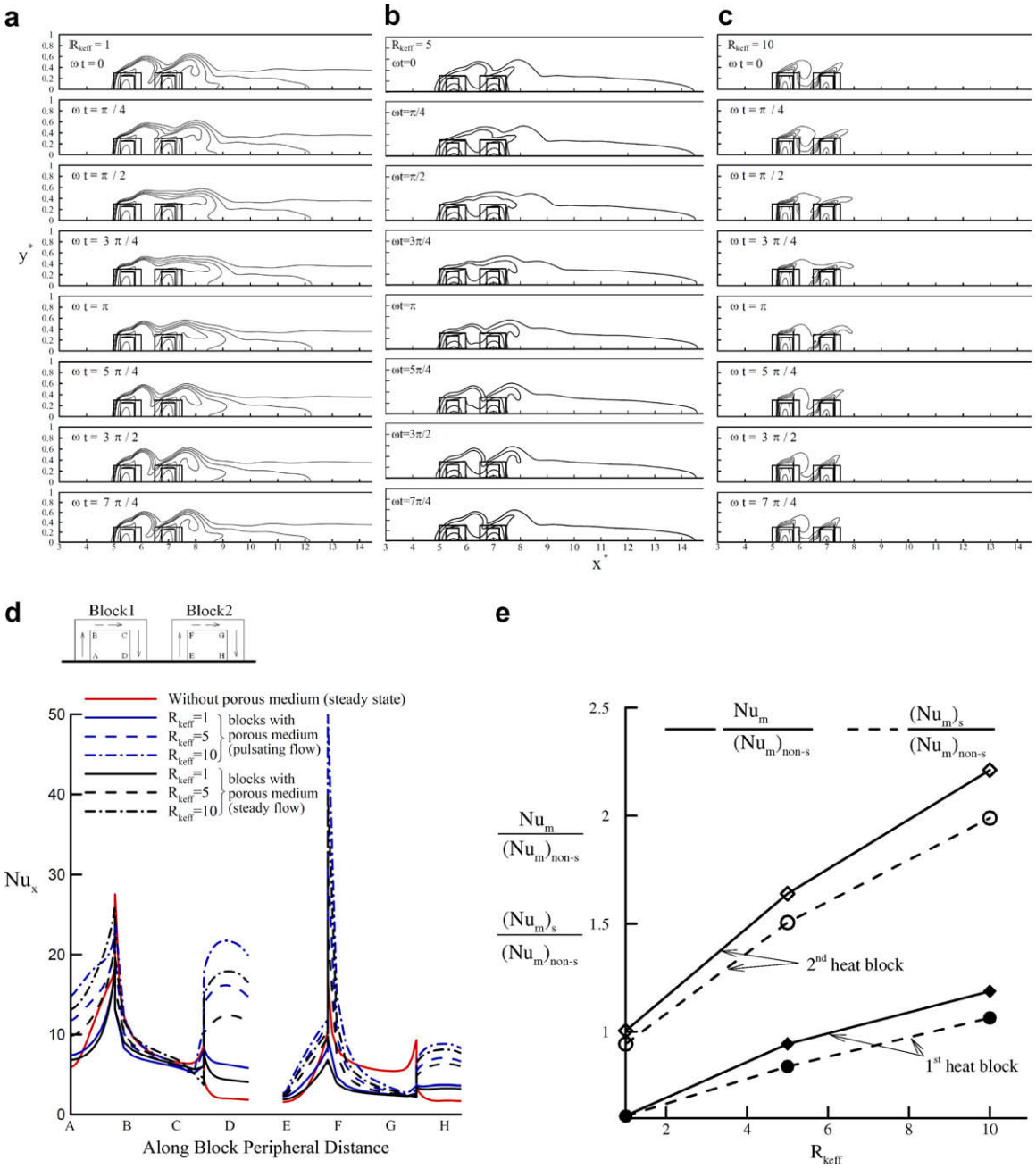

Fig. 11. Effects of the effective conductivity ratio on the variations of isotherms ($\Delta T^* = 0.1$) (a)–(c), cycle-averaged local Nusselt number (d), and heat transfer enhancement factor (e) during a periodic-steady cycle.

while slightly increases with the increase of the St from 0.4 to 1.0. The effect of St on the cycle-averaged local Nusselt number distribution Nu_x is shown in Fig. 7(d). It can be seen that an increase in St from 0.1 to 0.4 results in slight increase in Nu_x, until an optimal St/ heat transfer rate (around $St \sim 0.4$ for first block and $St \sim 0.6$ for second block) is reached and then decreases afterward. There are two reasons for this trend: the first season is that increasing Strouhal number causes heat penetrating distance into the fluid and the oscillation of this depth during a cycle to decrease, and the second is that the stronger oscillating interaction, caused by recirculations between the core flow and the heated block surface, convects more thermal energy away from the heated block. The increasing rate of heat transfer is up to a maximum and then decreases to a fixed value due to the reduction in the above-mentioned oscillating interaction between the core flow and the heated block surface. Again, as St increases, the gain in $Nu_m/(Nu_m)_{non\text{-}s}$ gradually increases to a maximum $Nu_m/(Nu_m)_{non\text{-}s} = 0.71$ for the first block around $St \sim 0.6$, and $Nu_m/(Nu_m)_{non\text{-}s} = 1.04$ for the second block around $St \sim 0.4$, as displayed in Fig. 7(e), and then decreases to a fixed value. The heat transfer enhancement factor is insensitive to the changes in the pulsating frequency when $St > 1.0$. For the first heater, the pulsating heat transfer enhancement factor $Nu_m/(Nu_m)_{non\text{-}s}$ is always larger than steady heat transfer enhancement factor $(Nu_m)_s/(Nu_m)_{non\text{-}s}$. For the second heater, $Nu_m/(Nu_m)_{non\text{-}s} > (Nu_m)_s/(Nu_m)_{non\text{-}s}$ only when $St > 0.2$. Also, the heater two has a larger heat transfer enhancement factors $Nu_m/(Nu_m)_{non\text{-}s}$ and $(Nu_m)_s/(Nu_m)_{non\text{-}s}$ than heater one in the estimated range of St.

4.6. Effects of the porous-covering geometric parameters H_p^*, W_p^*, and S_s^*

The porous-covering geometric parameters H_p^*, W_p^*, and S_s^* are related to the porous-covering block height, width, and spacing, respectively. The effects of varying porous-covering block height

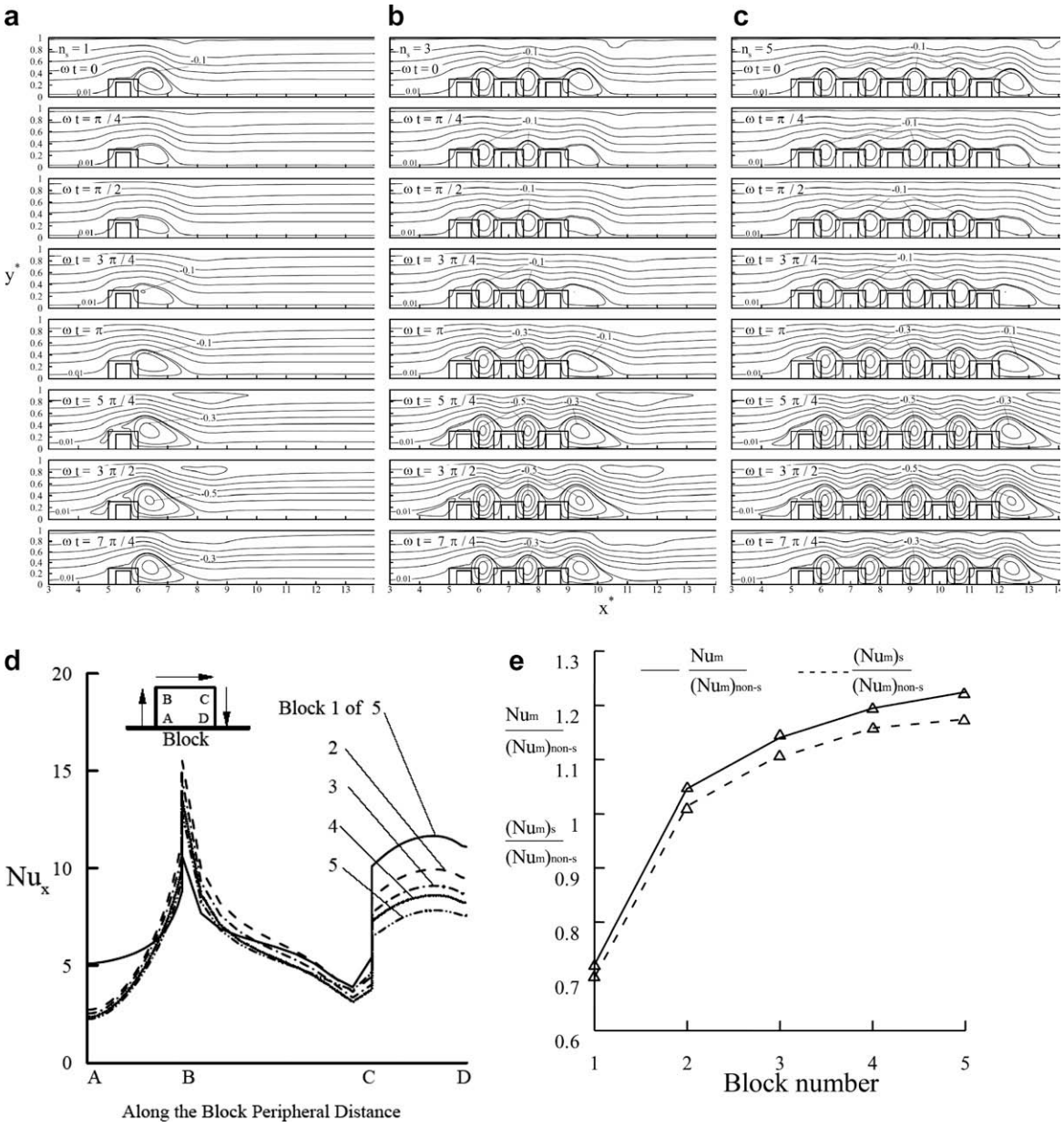

Fig. 12. Effects of the number of porous-covering heated blocks in a array on the variations of streamlines ($\Delta\varphi^* = 0.2$ for $0 < \varphi^* < 1$) (a)–(c), cycle-averaged local Nusselt number (d), and heat transfer enhancement factor (e) during a periodic-steady cycle.

H_p^* from 0.3 to 0.4 is shown in Fig. 8 for $W_p^* = 1.0$, $Da = 5 \times 10^{-5}$, $Re = 250$, $A = 0.4$, $St = 0.6$, $S_s^* = 1.0$, $H_s^* = 0.25$, $W_s^* = 0.5$, $R_{keff} = 1$, and $R_{ks} = 10$. In Fig. 8(a)–(c), it is seen that the distortions of instantaneous streamlines become evident. In addition, the size and strength of recirculation zones increase. This is the direct result of the increase in the porous-covering thickness above the top face of solid block, which in turn offers a higher degree of obstruction to the flow and subsequent grows the blowing action. The effect of increasing porous-covering block width from $W_p^* = 0.8$ to $W_p^* = 1.2$ is illustrated in Fig. 9 for $H_p^* = 0.3$, $Da = 5 \times 10^{-5}$,

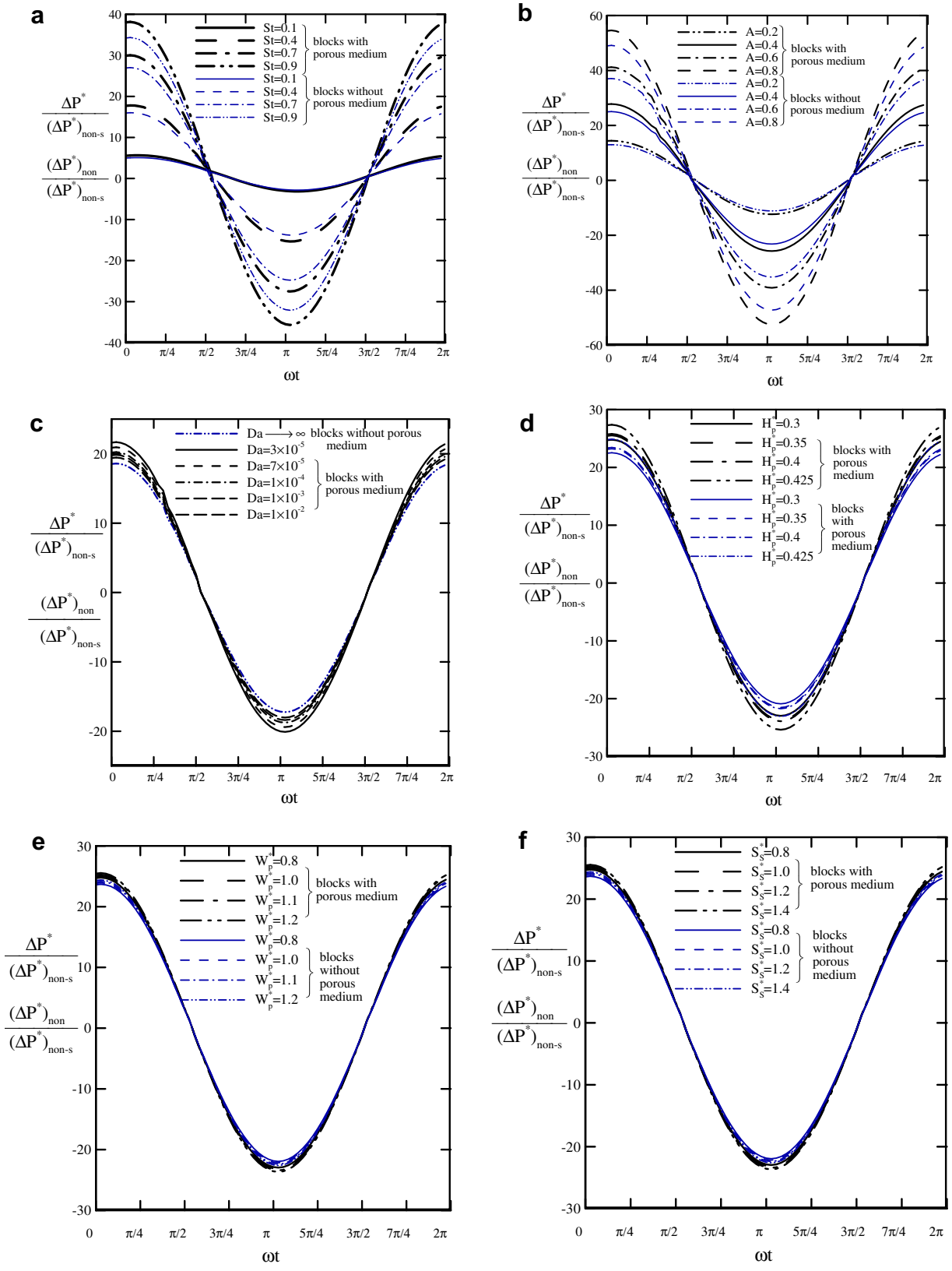

Fig. 13. The variations of temporal pressure drop factor along the upper plate for various values of (a) *St*, (b) *A*, (c) *Da*, (d) H_p^*, (e) W_p^*, and (f) S_s^*.

$Re = 250$, $A = 0.4$, $St = 0.6$, $S_s^* = 1.0$, $H_s^* = 0.25$, $W_s^* = 0.5$, $R_{keff} = 1$, and $R_{ks} = 10$. The wider porous-covering block width bring about smaller interblock recirculation because of the smaller volume of interblock cavity, as shown in Fig. 9(a)–(c). The effects of increasing the porous-covering block spacing S_s^* from 0.8 to 1.4 are shown in Fig. 10 for $Da = 5 \times 10^{-5}$, $Re = 250$, $A = 0.4$, $St = 0.6$, $H_s^* = 0.25$, $W_s^* = 0.5$, $H_p^* = 0.3$, $W_p^* = 1.0$, $R_{keff} = 1$ and $R_{ks} = 10$. As S_s^* increases from 0.8 to 1.2, the size of interblock recirculation zones increases (as shown in Fig 10(a) and (b)), and reduces as S_s^* is increased further to 1.4. When $S_s^* > 1.2$, the wider block spacing produces the flatter-and-wider instantaneous interblock recirculation, whose center moves to downstream wall of interblock cavity. This is because the larger block spacing allows more fluid into the interblock cavity, which, in turn, causes acceleration in the core flow and lessens the blowing action made by porous medium.

Figs. 8(d), 9(d), and 10(d) show the variation of Nu_x with geometric parameters H_p^*, W_p^*, and S_s^*, respectively. As expected, the larger interblock and downstream recirculations produce higher heat transfer rate from the block left (EF) and right (CD, GH) faces to the core flow by convection, but reduces at the block top faces (BC, FG). It is noticed that the relative large recirculating cell in front of the first block will increase the cycle-average local Nusselt number along its left face (AB), which depends on the porous-covering thickness at that face. As shown in Figs. 8(c) and 9(c), the heat transfer enhancement factor increases with increasing porous-covering obstacle height H_p^*, but decreases with increasing porous-covering obstacle width W_p^*. While the effect of inter-block spacing on the heat transfer enhancement factor does not go straight ahead. As S_s^* increases, the heat transfer enhancement factor gradually increases to a maximum value 0.74 for the first block around $S_s^* \sim 1.2$, and 1.04 for the second block around $S_s^* \sim 1.0$, as displayed in Fig. 10(c), and then decreases.

4.7. Effects of the effective thermal conductivity ratio R_{keff}

The effect of the effective thermal conductivity ratio is shown in Fig. 11 for fixed values of $Da = 5 \times 10^{-5}$, $Re = 250$, $A = 0.4$, $St = 0.6$, $S_s^* = 1.0$, $H_s^* = 0.25$, $W_s^* = 0.5$, $H_p^* = 0.3$, and $W_p^* = 1.0$, with $R_{keff} = 1$, 5, and 10, respectively. The values for the effective thermal conductivity ratio – 1, 5, and 10 – are such that they will cover a moderate range of thermophysical porous-material properties, which may correspond to certain nonmetallic materials [27]. Since Da, Re, A, and St are fixed, the variation of the effective conductivity ratio has no effect on the flow field, and therefore, the flow field is the same for all effective conductivity ratios. This pulsating flow field is shown in Fig. 4(a). As expected, increasing R_{keff} decreases the thickness of the thermal boundary layer at each time instant, as shown in Fig. 11(a)–(c). As seen in Fig. 11(d) the cycle-averaged local Nusselt numbers Nu_x along the block surfaces increase with an increase in the effective conductivity ratio R_{keff}. Fig. 11(e) gives the results for cycle-space average overall block mean Nusselt numbers. It can be seen that as R_{keff} increases the gain in $Nu_m/(Nu_m)_{non\text{-}s}$ increases significantly.

4.8. Effects of the number N_s of porous-covering blocks in the array

To examine whether the Nusselt numbers become periodic within the array, the baseline case was extended to five identical, porous-covering heated blocks with dimensions $S_s^* = 1.0$, $H_s^* = 0.25$, $W_s^* = 0.5$, $H_p^* = 0.3$, and $W_p^* = 1.0$, for $Re = 250$, $Da = 5 \times 10^{-5}$, $A = 0.4$, $St = 0.6$, $R_{keff} = 1.0$, $L_i^* = 5$, and $L_o^* = 25$. Fig. 12 gives the results for the flow fields, exposed surface cycle-average local Nusselt number, and heat transfer enhanced factors. Comparison of the instantaneous streamlines in Fig. 12(a)–(c) shows the distortion of streamlines becomes pronounced as the block number increases. Both strength and size of the instantaneous interblock recirculations are almost the same no matter what the number of block is 3 or 5 due to the same blowing strength occurring at the top face of each block. For the left, top, and right faces in the five-heated-block array, Nu_x decreases for downstream blocks except block one. This is because as the fluid passed over the heated blocks, the temperature of the fluid increases, which results in Nu_x decreases progressively for downstream blocks. It can be seen from Fig. 12(e) that the gain in $Nu_m/(Nu_m)_{non\text{-}s}$ and $(Nu_m)_s/(Nu_m)_{non\text{-}s}$ increases downstream the heat block array. The pulsating heat transfer enhancement factor $Nu_m/(Nu_m)_{non\text{-}s}$ is always larger than steady heat transfer enhancement factor $(Nu_m)_s/(Nu_m)_{non\text{-}s}$.

4.9. Pressure drop calculation

When using both inducing pulsation and porous material for augmenting heat transfer, an important factor to consider is the penalty arising from increased pressure drop. In the stream function-vorticity formulation, the pressure field is eliminated in obtaining the solution. However, the pressure field can be recovered from the converged stream function and vorticity fields. This is done by integrating the pressure gradient along the upper channel wall. The temporal pressure gradient in a periodic steady state is derived from the unsteady momentum equation using the no-slip boundary conditions on the solid wall. The total temporal pressure drop ΔP^* along the upper channel wall is then obtained from

$$\Delta P^* = \int_0^{L_t^*} \left.\frac{\partial P^*}{\partial x^*}\right|_{y^*=1} dx^* = -\int_0^{L_t^*} \left.\left[\frac{\partial u^*}{\partial t^*} + \frac{1}{Re}\frac{\partial \xi^*}{\partial y^*}\right]\right|_{y^*=1} dx^* \tag{19}$$

The corresponding steady non-pulsating nonporous-covering pressure drop $(\Delta P^*)_{non\text{-}s}$ is

$$(\Delta P^*)_{non\text{-}s} = \int_0^{L_t^*} \left.\frac{\partial P^*}{\partial x^*}\right|_{y^*=1} dx^* = -\int_0^{L_t^*} \left.\frac{1}{Re}\frac{\partial \xi^*}{\partial y^*}\right|_{y^*=1} dx^* \tag{20}$$

where pressure P^* is non-dimensionalized with respect to ρu_o^2. The effects of Da, A, St, H_p^*, W_p^*, and S_s^* on the temporal pressure drop factor $\Delta P^*/(\Delta P^*)_{non\text{-}s}$ and $(\Delta P^*)_{non}/(\Delta P^*)_{non\text{-}s}$, which gives the overall pressure drop with and without the porous covers, respectively, throughout the entire channel length, normalized by the corresponding steady non-pulsating nonporous-covering value $(\Delta P^*)_{non\text{-}s}$, is presented in Fig. 13. In Fig. 13(e) and (f) the amplitude of the temporal pressure drop factor is less affected by a change in W_p^* (at $Re = 250$, $Da = 5 \times 10^{-5}$, $A = 0.4$, $St = 0.6$, $S_s^* = 1.0$, $H_s^* = 0.25$, $W_s^* = 0.5$, and $H_p^* = 0.3$), and or S_s^* (at $Re = 250$, $Da = 5 \times 10^{-5}$, $A = 0.4$, $St = 0.6$, $H_s^* = 0.25$, $W_s^* = 0.5$, $H_p^* = 0.3$, and $W_p^* = 1.0$). However, the magnitude of $\Delta P^*/(\Delta P^*)_{non\text{-}s}$ increases substantially as St (at $Re = 250$, $Da = 5 \times 10^{-5}$, $A = 0.4$, $S_s^* = 1.0$, $H_s^* = 0.25$, $W_s^* = 0.5$, $H_p^* = 0.3$, and $W_p^* = 1.0$) or, A (at $Re = 250$, $Da = 5 \times 10^{-5}$, $St = 0.6$, $S_s^* = 1.0$, $H_s^* = 0.25$, $W_s^* = 0.5$, $H_p^* = 0.3$, and $W_p^* = 1.0$), *and or* H_p^* (at $Re = 250$, $Da = 5 \times 10^{-5}$, $A = 0.4$, $St = 0.6$, $S_s^* = 1.0$, $H_s^* = 0.25$, $W_s^* = 0.5$, and $W_p^* = 1.0$) increases, *and or* as Da (at $Re = 250$, $St = 0.6$, $A = 0.4$, $S_s^* = 1.0$, $H_s^* = 0.25$, $W_s^* = 0.5$, $H_p^* = 0.3$, and $W_p^* = 1.0$) decreases, as seen in Fig. 13(a)–(d). The reason is that as the flow approaches the smaller passage formed by the porous-covering blocks and the upper surface of the channel, the fluid starts to accelerate, resulting in an increase in the pressure drop. The temporal pressure recovery behind each porous-covering block is not complete due to the pressure loss in the recirculation zones. A decrease in Da or increase in H_p^* provides a larger bulk frictional resistance to flow and grows the blowing action. This in turn enhances the growth of recirculation zones in the transverse direction, resulting in a profound increase in variations of temporal pressure drop. An increase in St or A also leads to a larger pressure loss due to the formation of stronger and larger recirculating zones in the channel

as stated previously. As expected, the temporal pressure drop factor $(\Delta P^*/(\Delta P^*)_{\text{non-s}})$ for porous-covering case is always larger than that $((\Delta P^*)_{\text{non}}/(\Delta P^*)_{\text{non-s}})$ for nonporous-covering case, as shown in Fig. 13. Therefore, the required pumping power to maintain a pulsating flow increases as pulsation amplitude, Darcy number and porous blockage ratio. The phase lead of temporal pressure gradient $\Delta P^*/(\Delta P^*)_{\text{non-s}}$ over the inlet pulsating velocity for all cases studied here is around $\pi/2$. This indicated that the flow pulsation considered in this study is in a higher frequency regime, compared to the oscillating flow inside a smooth duct [24]. In this classical oscillating flow, the phase leads of pressure drop over the inlet velocity approaches $\pi/2$ from zero as ω increases.

5. Conclusions

This study presents a numerical simulation of forced pulsating convective flow in a parallel-plate channel with tandem porous-covering heated blocks. Findings indicate that for the case of non-pulsating steady flow the heat transfer rate from the right face of block heaters could be enhanced by fiber porous-covering heat sink, which depends on the consolidated result of four interrelated effects caused by porous block: penetrating, blowing, suction and boundary layer separation. For the case of pulsating flow, the steady and stable flow field is substantially destabilized by external pulsation and exhibits a cyclic expanding and shrinking alteration of the vortex structure. The phase diagrams also show that this unsteady pulsating flow is highly periodic and well organized. The temperature field is significantly affected by such increased large-scale flow mixing and presents a periodic oscillation of the thermal boundary layer thickness near the heater surfaces. It is shown the heat transfer enhancement factor $Nu_m/(Nu_m)_{\text{non-s}}$ of the block heaters increases with the pulsating amplitude, height of porous-covering obstacle, and effective conductivity ratio, but decreases with width of porous-covering obstacle. However, the effects of Darcy number, Strouhal number, and spacing of porous-covering obstacle are not straightforward. There exists a critical value for which the heat transfer enhancement factor is minimum (for Darcy numbers) or maximum (for Strouhal number and obstacle spacing). Below and above this critical value, the heat transfer enhancement factor drops off or goes up. Under specific choices of descriptive parameters, the value of pulsating heat transfer enhancement factor $Nu_m/(Nu_m)_{\text{non-s}}$ is larger than that of steady heat transfer enhancement factor $(Nu_m)_s/(Nu_m)_{\text{non-s}}$. In addition, although using the porous-covering heat sink can significantly enhance the heat transfer rate on the block right face, it also leads to a decrease on the frontal and upper sides of the blocks (especially the upstream block one). This can be improved by using (1) high-conductivity porous heat sink, and (2) porous layer covering the second block but just partially covering the first block [27]. This may also decrease the pressure drop.

The results of this investigation clearly demonstrate that the heated block with high-conductivity fiber porous-covering heat sink subjected to forced pulsating channel flow is an effective method for cooling electronic devices. However, one must consider a tolerance limit in view of increased pressure drop to determine the optimal amplitude of external pulsation according to the porous blockage ratio and porous material.

Acknowledgements

This work was supported by the R.O.C. National Science Council and Ministry of Economic Affairs, Bureau of Energy under Contracts NSC 94-2212-E-027-021 and 97-D0137-3.

References

[1] J.C.Y. Koh, R. Colony, Analysis of cooling effectiveness for porous material in a coolant passage, ASME J. Heat Transfer 96 (1974) 324–330.
[2] M. Kaviany, Laminar flow through a porous channel bounded by isothermal parallel plate, Int. J. Heat Mass Transfer 28 (1985) 851–858.
[3] P.C. Huang, K. Vafai, Analysis of forced convection enhancement in a parallel plate using porous blocks, AIAA J. Thermophys. Heat Transfer 18 (1994) 563–573.
[4] D. Angirasa, Forced convective heat transfer in metallic fibrous materials, ASME J. Heat Transfer 124 (2002) 739–745.
[5] H.A. Hadim, A. Bethancourt, Numerical study of forced convection in a partially porous channel with discrete heat sources, ASME J. Heat Transfer 8 (1995) 465–472.
[6] D. Angirasa, G.P. Peterson, Forced convection heat transfer augmentation in a channel with a localized heat source using metal fibrous material, ASME J. Electron. Packaging 121 (1999) 1–7.
[7] W.S. Fu, H.C. Huang, W.Y. Liou, Thermal enhancement in laminar channel flow with a porous block, Int. J. Heat Mass Transfer 39 (1996) 2165–2175.
[8] P.C. Huang, C.F. Yang, J.J. Hwang, M.T. Chiu, Enhancement of forced-convection cooling of multiple heated blocks in a channel using porous covers, Int. J. Heat Mass Transfer 48 (2005) 647–664.
[9] M.R. Mackley, X. Ni, Mixing and dispersion in a baffled tube for steady laminar and pulsatile flow, Chem. Eng. Sci. 46 (1991) 3139–3151.
[10] T. Nishimura, S. Murakami, Y. Kawamura, Heat transfer in a symmetric sinusoidal wavy-walled channel for oscillatory flow, in: Proceedings of the Second JSME-KSME Thermal Engineering Conference, 1992, pp. 89–94.
[11] K. Azar, Enhanced cooling of electric components by flow oscillation, AIAA J. Thermophys. Heat Transfer 6 (1992) 700–706.
[12] S.Y. Kim, B.H. Kang, J.M. Hyun, Heat transfer from pulsating flow in channel filled with porous media, Int. J. Heat Mass Transfer 37 (1994) 2025–2033.
[13] J.M. Khodadadi, Oscillatory fluid flow through a porous medium channel bounded by two impermeable parallel plates, J. Fluid Eng. 113 (1991) 509–511.
[14] J.W. Paek, B.H. Kang, J.M. Hyun, Transient cool-down of a porous medium in pulsating flow, Int. J. Heat Mass Transfer 42 (1999) 3523–3527.
[15] H.L. Fu, K.C. Leong, C.Y. Liu, An experimental study of heat transfer of a porous channel subjected to oscillating flow, ASME J. Heat Transfer 110 (2001) 946–954.
[16] K.C. Leong, L.W. Jin, An experimental study of heat transfer in oscillating flow through a channel filled with aluminum foam, Int. J. Heat Mass Transfer 48 (2005) 243–253.
[17] Z. Guo, S.Y. Kim, H.Y. Sung, Pulsating flow and heat transfer in a pipe partially filled with a porous medium, Int. J. Heat Mass Transfer 40 (1997) 4209–4218.
[18] M.L. Hunt, C.L. Tien, Effects of thermal dispersion on forced convection in fibrous media, Int. J. Heat Mass Transfer 31 (1988) 301–310.
[19] K. Vafai, C.L. Tien, Boundary and inertial effects on flow and heat transfer in porous media, Int. J. Heat Mass Transfer 24 (1981) 195–203.
[20] P.C. Huang, S.H. Nian, C.F. Yang, Enhanced heat-source cooling by flow pulsation and porous block, AIAA J. Thermophys. Heat Transfer 19 (2005) 460–470.
[21] J. Adams, J. Ortega, A multicolor SOR method for parallel computation, in: Proceedings of the International Conference on Parallel Procession, 1982, pp. 53–56.
[22] S.W. Patankar, Numerical Heat Transfer and Fluid Flow, McGraw-Hill, New York, 1980.
[23] G. Neale, W. Nader, Practical significance of Brinkman's extension of Darcy's law coupled parallel flows within a channel and a bounding porous medium, Can. J. Chem. Eng. 52 (1974) 475–478.
[24] H. Schlichting, Boundary-Layer Theory, McGraw-Hill, New York, 1979.
[25] S.Y. Kim, B.H. Kang, Forced convection heat transfer from two heated blocks in pulsating channel flow, Int. J. Heat Mass Transfer 41 (1998) 625–634.
[26] H.J. Sung, S.Y. Kim, J.M. Hyun, Forced convection from an isolated heat source in a channel with porous medium, Int. J. Heat Fluid Flow 16 (1995) 527–535.
[27] R. Rachedi, S. Chikh, Enhancement of electronic cooling by insertion of foam materials, Heat Mass Transfer 37 (2001) 371–378.